Brigham Young University

BYU ScholarsArchive

2024-12-18

Grain Boundary Solute Segregation Across the 5D Space of Crystallographic Character

Lydia Harris Serafin
Brigham Young University

Follow this and additional works at: https://scholarsarchive.byu.edu/etd

Part of the Physical Sciences and Mathematics Commons

Grain Boundary Solute Segregation Across the 5D Space

of Crystallographic Character

Lydia Harris Serafin

A thesis submitted to the faculty of
Brigham Young University
in partial fulfillment of the requirements for the degree of

Master of Science

Eric Homer, Chair
Gus Hart
Mark Transtrum

Department of Physics and Astronomy

Brigham Young University

ABSTRACT

Grain Boundary Solute Segregation Across the 5D Space
of Crystallographic Character

Lydia Harris Serafin
Department of Physics and Astronomy, BYU
Master of Science

Solute segregation in materials with grain boundaries (GBs) has emerged as a popular method to thermodynamically stabilize nanocrystalline structures. However, the impact of varied GB crystallographic character on solute segregation has never been thoroughly examined. This work examines Co solute segregation in a dataset of 7272 Al bicrystal GBs that span the 5D space of GB crystallographic character. Considerable attention is paid to verification of the calculations in the diverse and large set of GBs. In addition, the results of this work are favorably validated against similar bicrystal and polycrystal simulations. As with other work, we show that Co atoms exhibit strong segregation to sites in Al GBs and that segregation correlates strongly with GB energy and GB excess volume. Segregation varies smoothly in the 5D crystallographic space but has a complex landscape without an obvious functional form.

ACKNOWLEDGMENTS

Contents

Chapter 1

Introduction

Solute atoms in polycrystalline materials with grain boundaries (GBs) may stay in the bulk, diffuse to the surface, or segregate to the GB, among other behaviors such as forming precipitates. When solute atoms segregate, they often remain in the GB network due to both kinetic mechanisms and thermodynamic stabilization. Some examples of kinetic mechanisms are solute drag that slows GB mobility [1] and solute pinning that prevents GB mobility under external driving forces [2]. Thermodynamic stabilization involves lowering the Gibbs free energy of a GB interface by the presence of the solute atom [3, 4], and is described in a theoretical framework developed by Weissmüller [5, 6]. Thermodynamic stabilization can be utilized to engineer materials with greater hardness than a pure material even at elevated temperatures (e.g., in [3, 7–9]) due to the Hall-Petch effect that causes greater hardness with smaller grain sizes [10, 11]. A recent review of thermodynamic stabilization is given in [12].

Early on, simple effective segregation energy models of solute segregation [13] were derived from experimentally determined values and are still often used to predict solute concentration at GBs and in larger mesoscale models [14–19].[1] However, such models violate the third law of thermodynamics [21], do not account for the effects of GB character on the system, and are

---

[1]Other models of segregation energy are reviewed in Chapter 4 of [20].

insufficient to describe experimental behavior [22–24], in particular of strong segregation to specific atom sites (e.g., in the Co-Al-W system [25]).

Recently, models that are informed by simulated data have been developed to address such issues. GB solute segregation has been examined in the dilute limit in atomistic studies utilizing polycrystals [21, 26–30] and bicrystals in small regions of the 5D GB space [31–36], as well as in first-principles [36–41] and experimental studies [42, 43]. Some studies improve on the segregation energy calculations by including entropic and other effects in the atomistic simulations [30, 44]. Others move beyond the dilute limit by considering solute-solute interactions [45], or multiple-solute interactions [46]. From these data, segregation models are often created using machine learning techniques [27, 31, 32], specifically to predict segregation energy of specific atom sites from their local environments. Recent reviews of computational modeling of solute segregation are given in [47, 48]. Here, we highlight two recent and notable efforts to create more accurate segregation energy models based on segregation energy spectra, which permits enforcement of the third law of thermodynamics [21].

Huber et al. created a small dataset of densely sampled $\Sigma 5$ coincident site lattice (CSL) Al bicrystal GBs and calculated segregation energy spectra for 6 different solute types to inform machine learning models for solute segregation at the atomic level [31]. They found that a thorough sampling of the 5D space of GB crystallographic character was necessary for the creation of a segregation energy spectrum that informs a model more accurate than the rudimentary effective segregation energy model. Wagih et al. [28] also point out issues with using an effective segregation energy for solute concentration models, demonstrated by the bimodal spectrum of segregation energies in the Pd-H system due to the occupation of interstitial sites. In response, they created solute segregation spectra in polycrystals for use in segregation energy models by performing atomistic simulations of Mg in Al polycrystals [26]. This polycrystal approach creates one segregation energy spectrum for the entire dataset, rather than many small spectra that are concatenated to

represent the dataset, as is necessary for bicrystal GBs. Wagih et al. used machine learning on these polycrystal spectra to inform 259 binary alloy system segregation models [27], as well as some quantum-accurate models [49].

Wagih et al. use polycrystal simulations in order to more fully capture the behavior of real materials, and they caution against using bicrystal simulations [26]. They suggest that only thorough samplings of bicrystal GBs in the 5D space of crystallographic character should be used for this purpose, promoting the work by Huber et al. in [31] as an example of sufficient sampling, albeit in a small subspace of the 5D space. Others have also noted the insufficiency of bicrystal GB simulations, such as Tucker et al. who use the strain functional description of atomic configurations to show that symmetric twist GBs (STGBs) cannot be used to represent polycrystals or amorphous structures [50]. Wagih et al. also present evidence that STGBs and low coincidence site lattice (CSL) GBs do not represent polycrystals generally [51].

In this work, we compute the segregation energy of 70 million Co atoms in 7272 Al bicrystal GBs from the Homer GB dataset [52]. The use of this dataset attempts to address most of the concerns raised about using bicrystal GBs simulations to inform GB solute segregation models in [26, 50, 51] because it spans the 5D space of GB crystallographic character. It is also not limited to STGBs or low CSL GBs; it includes CSL values up to $\Sigma 999$. Additionally, the use of this dataset is a step towards examining the behavior of solute segregation across the entire GB space, which is noted as an important next step for the field [48], since segregation has been found to depend on GB character [53]. Co is used as a solute in this work because of its use in similar works [27, 31], because Al-Co alloys can be used in a wide variety of applications [54], and because Co additions in small quantities can mitigate challenges in 3D printing of otherwise pure Al [55]. However, the methods and analysis described in this work could be repeated with other solvent-solute combinations. We verify and validate the resulting data, including direct comparisons to the works by Huber et al. in [31] and Wagih et al. in [27]. Finally, we examine the spectra using several techniques, including

a statistical overview, a classification scheme, and reduction to a solute concentration for each GB, and we identify some subsets of GBs that deviate significantly from the mean solute concentration.

Chapter 2

Methods

2.1 Theory of solute segregation

The segregation energy E_{seg} of an atom is defined as the energy difference between a solute atom and a solvent atom at the same site in the GB minus the same energy difference at a reference atom site located in bulk [20, 26]. In this work, we examine the segregation of Co in Al, which is calculated according to:

$$E_{\text{seg}}^{\text{Co}_i} = \left(E_{\text{Co}}^i - E_{\text{Al}}^i\right) - \left(E_{\text{Co}}^{\text{ref}} - E_{\text{Al}}^{\text{ref}}\right) \tag{2.1}$$

where E_{Co}^i is the energy of a Co atom in the i-th atomic site in a GB, E_{Al}^i is the energy of an Al atom in the i-th atomic site, and $E_{\text{Co}}^{\text{ref}}$ and $E_{\text{Al}}^{\text{ref}}$ are the energies for a reference atom in bulk, far away from the GB.[1] All of these values are calculated at 0 K. In this formulation, segregation is energetically favorable for a site when $E_{\text{seg}}^{\text{Co}_i}$ is negative.

---

[1]Equation 2.1 is an approximation for the free energy or enthalpy change due to the solute segregation at the grain boundary. This formulation is only valid in the dilute limit, since it neglects solute-solute interactions [56].

2.2 Solute segregation energy spectrum creation

In this work, segregation energy data is collected by substituting single Co atoms into Al GBs from a dataset created by Homer et al. [52, 57] which used the pure Al EAM potential from Mishin et al. [58]. This dataset is referred to in the present work as the Homer dataset. The Homer dataset contains GB structures that have 150 different CSL values corresponding to unique disorientations up to Σ999, sampled at intervals of ∼5° in the disorientation space. For each CSL value, a sampling of boundary planes (BPs) was selected to provide comprehensive coverage, making 7304 unique GBs in the 5D space of GB crystallographic character.[2] The optimal atomic configuration for each GB was then found by varying 6 parameters of GB construction while maintaining the 5D constraint of the GB, relaxing each structure via conjugate gradient energy minimization. In this work we examine only the minimum energy configuration of the 6 GB construction parameters. See [57] for additional details about the construction of the Homer dataset.

Segregation energy values in Equation 2.1 were computed in LAMMPS molecular statics simulations [59] using the Ni-Al-Co empirical EAM potential from Purja Pun et al. [60], which is the same potential used by Huber et al. in [31] and Wagih et al. in [27]. Note that Co is known to develop a magnetic moment [61], but this EAM potential has been carefully fitted to the Al-Co phase diagram [60] and all our calculations are with individual Co atoms so we assume that magnetic effects are negligible and can be disregarded in this work. In addition, this potential reproduces similar GB behavior to the Mishin potential ([58]) used in the creation of the GB dataset. We start with a relaxed GB structure and replace an existing Al atom with a Co atom at the same atom site. The entire GB structure is then relaxed via conjugate gradient minimization to an energy and force tolerance of 10^{-10} relative error and 10^{-10} eV/Å, respectively. Following minimization, the segregation energy for the substituted atom, $E_{\text{seg}}^{\text{Co}_i}$, is calculated using Equation 2.1.

---

[2]10 of the 7304 GB structures in the Homer dataset [52] are excluded from this work due to computational difficulties. See Supplemental Table S3 for a list of excluded GBs.

This process was completed for approximately 70 million atoms from 7272 GBs: each atom closer than 15 Å to the GB plane was replaced by a Co atom, as well as a random sample of 100 atoms for each GB in the range of 15–25 Å to use for bulk reference energies ($E_{\text{Co}}^{\text{ref}}$ & $E_{\text{Al}}^{\text{ref}}$). Atoms further away from the GB are not substituted because $E_{\text{seg}}^{\text{Co}_i}$ rapidly falls to 0 eV with distance from the GB plane [62,63].

2.3   Analysis techniques

Since the segregation data for each GB results in a spectrum of values, we employ two methods to simplify comparison of the spectra across the set of GBs. Specifically, these methods are i) a classification scheme and ii) a grain boundary solute concentration, which are described below.

For reasons that will be clear in the verification section (3.1), we implement a classification scheme that classifies any atom with near-bulk segregation behavior as "negligibly segregating." We do this because the segregation energy values of the bulk atoms actually take on a range of values about 0 eV and GB atoms with segregation energy values in that same range would behave the same as if they were in bulk. We designate segregation energy values in the 95% interval[3] of the bulk atom distribution as "negligibly segregating". This allows us to more easily determine which atoms are "segregating" and "anti-segregating" because they are outside the range of typical bulk atom segregation energies. The ranges for these three possible classifications are: i) segregating; $E_{\text{seg}}^{\text{Co}_i} < -0.0875$ eV, ii) negligibly segregating; -0.0875 eV $\leq E_{\text{seg}}^{\text{Co}_i} < +0.018$ eV, and iii) anti-segregating; $E_{\text{seg}}^{\text{Co}_i} \geq +0.018$ eV.

A standard measure of solute segregation at GBs is the solute concentration at the GB in the dilute limit, c_{GB}. Early literature calculated this value using a single effective segregation

---

[3]Supplemental Figure S3 shows a number of intervals on the distribution of FCC atoms, from which we determined to use a 95% interval for the "negligible" classification. Supplemental Figure S4 shows a number of intervals on the distribution of non-FCC atoms.

energy [13] or a continuous distribution of segregation energies for atoms in the GB [64]. This type of approach is computationally simple but has some pitfalls (as mentioned in Section 1) that can be avoided by using a discrete segregation energy spectrum. Coghlan and White first created such a spectrum [22], which was later adapted by Huber et al. [31] for an array of individually described atoms in a single GB. The concentration of solute atoms in the GB is then calculated according to:

$$c_{GB} = \frac{1}{N} \sum_i \left[1 + \frac{1 - c_{bulk}}{c_{bulk}} \exp\left(E_{seg}^{Co_i} / k_B T \right) \right]^{-1} \tag{2.2}$$

where $E_{seg}^{Co_i}$ is defined by Equation 2.1, N is the number of sites in the GB, k_B is the Boltzmann constant, T is the temperature, and c_{bulk} is the concentration of solute in bulk, held fixed as an independent variable. Bulk atom sites are chosen for solute occupancy at finite temperatures with increasing probability, lowering c_{GB}; the temperature dependence of this value is demonstrated for this work in Section 4, and is a well known feature of GB segregation [65]. The $\frac{1 - c_{bulk}}{c_{bulk}}$ term scales the Fermi level down as bulk atom sites are filled at finite temperatures, as discussed in [31]. In this work we use a bulk concentration of $c_{bulk} = 0.2$ at.%, chosen to be the same as in Huber et al. [31].

Chapter 3

Verification and Validation

An important step in collection of any data is the verification and validation of the results [66]. In the following sections we verify that the calculated values are representative of true segregation energies and validate the results by comparing them to other published examples.

3.1   Verification

In verifying the data collected in this work, we noted that some data was incorrect or did not match expected behavior. The following sections discuss the process of determining which data could be verified for accuracy and inclusion in the work.

Verification of bulk segregation energies

By definition (Equation 2.1), solute atoms in the bulk have segregation energies of 0 eV. In order to verify this behavior, we must classify atoms as either bulk or GB atoms. The method by which the GB atoms are separated from the bulk atoms will have an impact on whether bulk atoms exhibit the expected 0 eV segregation energy. Since a segregation energy spectrum typically only includes

GB atoms, the classification scheme can also affect the segregation energy spectra based on the inclusion of atoms near or in the GB that may or may not have segregation energies near 0 eV.

Bulk atoms are often identified in simulations by adaptive common neighbor analysis (aCNA), as employed in [26–28, 30–33], which can identify each atom's environment as HCP, BCC, ICO, FCC or other [67]. Alternatively, the centrosymmetry parameter (CSP) [68] can be used to identify atom environments where the expected centrosymmetry breaks down, such as near a GB in an FCC-type crystal structure. In bicrystal simulations, a simple identification method is to categorize atoms within some fixed width (e.g. ± 5Å) of the center of the GB as belonging to the GB. There are several less commonly used methods to determine bulk atoms, such as the dislocation extraction algorithm (DXA) [69, 70] used in [42], the per-site Voronoi volume criterion used in [35], and the experimentally determined one-atomic layer region from the GB center [71, 72], as employed in [29].

There are challenges with using aCNA, CSP, and DXA as classification methods because they were designed for purposes other than determining whether an atom belongs to a GB. The aCNA method excels at structure identification, but tolerates distortions of atoms in those structures. The CSP method, since it is continuous, is better suited to differentiate smaller distortions. However, it has no defined cutoff value for discerning when a distortion has changed the structure sufficiently to be classified as something other than FCC, which is left for the user to choose. The fixed width method does not generalize easily to polycrystal simulations, and due to relaxation in the positions of atoms near the initial position of the GB plane, defining the center of the GB can be difficult, especially in the case of GB faceting. Additionally, the width of the GBs across a single dataset can very drastically (e.g. in ref [57], Figure 5 shows that the width of GBs in the Homer dataset range from 3-18Å, and the selection of a single fixed width would bias the number of FCC atoms included). The experimentally determined one-atomic layer region from the GB center is difficult to compare to simulations. The other methods suffer from similar challenges. There is no clear way to

determine whether an atom definitively belongs to the GB because the transition from bulk to GB can be subtle; elastic strains that cause some deviation from a "perfect" bulk structure are present even at large distances.

These challenges and the differences between the most commonly used methods of aCNA and CSP classification are illustrated in Figure 3.1 for a) a [100] symmetric tilt GB with an array of edge dislocations and for b) a high-angle GB. The atoms are colored according to their segregation energy value (red for anti-segregating, blue for segregating, grey for negligible). The figure depicts the full structure of the GB in the "All atoms" row, and the removal of more and more of the surrounding atoms depending on the CSP value used to remove "bulk" atoms. The "CNA" row shows that the aCNA is aggressive in its removal of "bulk" atoms, since its goal is not to identify local distortions in structure but clear changes in crystal structure. The result is that many surrounding atoms with non-negligible segregation energy values are removed by aCNA bulk determination.

Figure 3.1 illustrates that there is no definitive approach to atom selection for 0 eV bulk GB segregation energies using aCNA or CSP. In this work, we present results for bulk atom selection using both aCNA and CSP methods to compare the impact the selection method has since the aCNA method removes many atoms that could meaningfully contribute to segregation energy spectra. We also show cumulative segregation energy spectra of several fixed width cutoffs in Supplemental Figures S5 and S6, where liberal width leads to CSP-like distributions and conservative width leads to aCNA-like distributions. In this work, CSP labeled results use a CSP cutoff of 0.1, as it includes a reasonable number of surrounding atoms with non-negligible values of the segregation energies while limiting the number of bulk atoms with negligible values of the segregation energy.

Supplemental Section S1 contains a discussion comparing bulk atom selection by the aCNA and CSP techniques. The discussion can be summarized in the segregation energy distributions of the bulk atoms by the two classification techniques shown in Figure 3.2. The majority of bulk atoms have segregation energy values close to 0 eV, though there is a larger than expected variation in
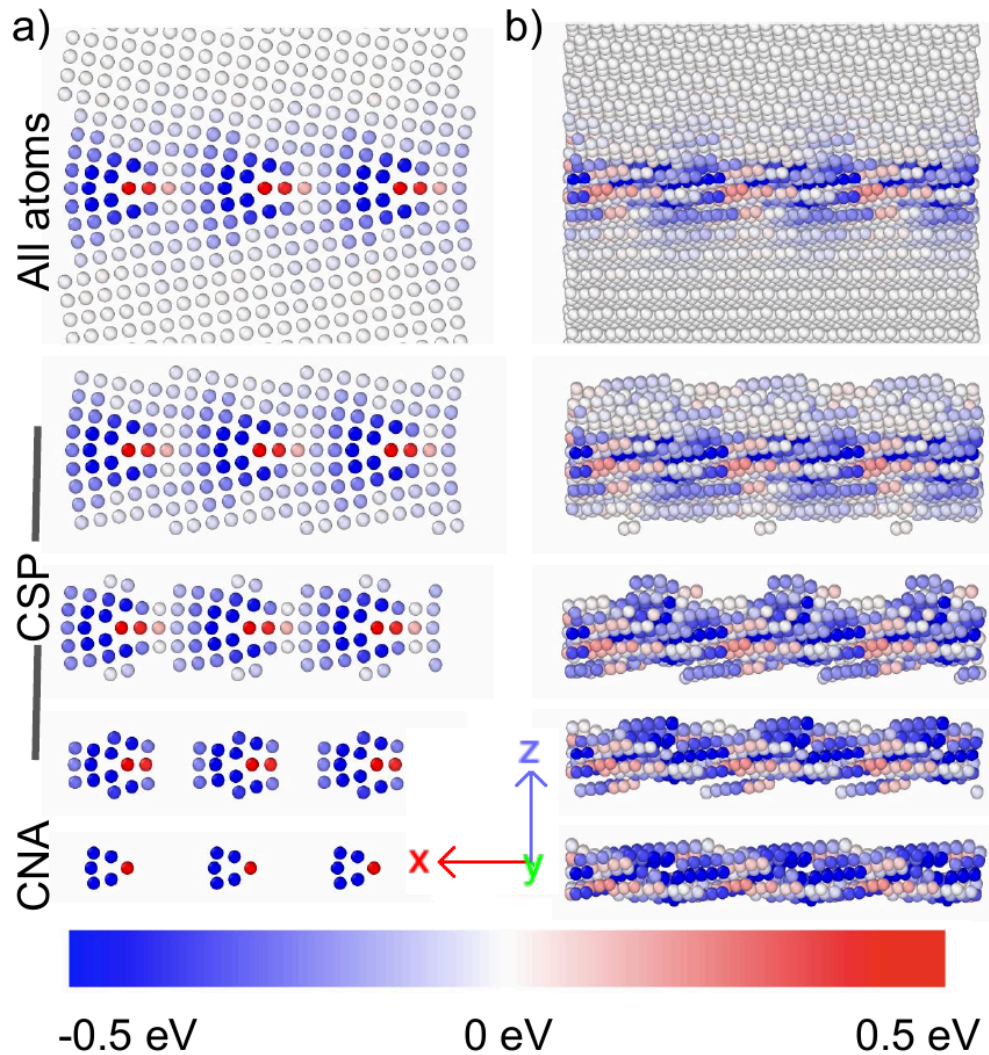
Figure 3.1 a) A [100] symmetric tilt GB with an array of edge dislocations and b) a high angle, low symmetry GB with "All atoms", "CSP" bulk atom removal (2nd row: CSP ≤ 0.3, 3rd row: CSP ≤ 0.1, 4th row: CSP ≤ 0.01), and adaptive "CNA" bulk atom removal. Red atoms have positive segregation energies, blue have negative, and grey have negligible, according to the colorbar shown. In both cases, the positive y-axis corresponds to the positive z-axis in the GB simulations, and the GB plane is located at $z = 0$Å. The crystallographic directions for each are given in Supplemental Table S2 . The GB images are produced using OVITO [73].

the local environments of bulk atoms as determined by both aCNA and CSP. In short, both bulk

atom classification schemes classify some atoms as bulk even though they have non-negligible

segregation energy values. Given the range of elastic strains near defects, it remains a challenge to find a single defensible method to identify GB and bulk atoms. By contrasting the aCNA and CSP bulk classification schemes in this work, we illustrate the difference between conservative and liberal classification schemes. The determination of a better method for selecting GB atoms is left for the community to resolve.

Recalling that theory defines segregation energy of an atom in the bulk as equal to 0 eV, one would expect segregation energies to converge to 0 eV as distance from the GB plane increases [62, 63]. In an initial analysis, it was found that while the majority of data behaved in this way, some did not converge to 0 eV more than 15 Å away from the GB plane. This is illustrated in a plot of segregation energy vs. distance from the GB plane in the scatter plot of Figure 3.3 for three different populations. These populations make up the 70 million atoms and are: the bulk atoms (gray), the GB atoms (blue), and atoms belonging to GBs excluded from the dataset because of errors described here and the following section (red). Four GBs in particular account for the scatter (non-zero segregation energy values) at large distance from the GB, and were therefore excluded from further analysis. These four GBs are listed in Supplemental Table S3 along with GBs excluded for reasons that are discussed in the next section. It can be seen in Figure 3.3 that their are still GB atoms at large distance from the GB, but in all cases these have segregation energy values near zero; furthermore, there are very few of these, so they contribute negligibly to the spectra of individual GBs.

Challenges due to GB restructuring

It can be seen in the red data points in Figure 3.3 that there are a small number of very negative segregation energy values, far below what would be expected for this system. When substituting a solute atom for segregation energy calculations, the energy of the new system is calculated after the system has relaxed into the new configuration that accommodates the solute atom. Usually, this
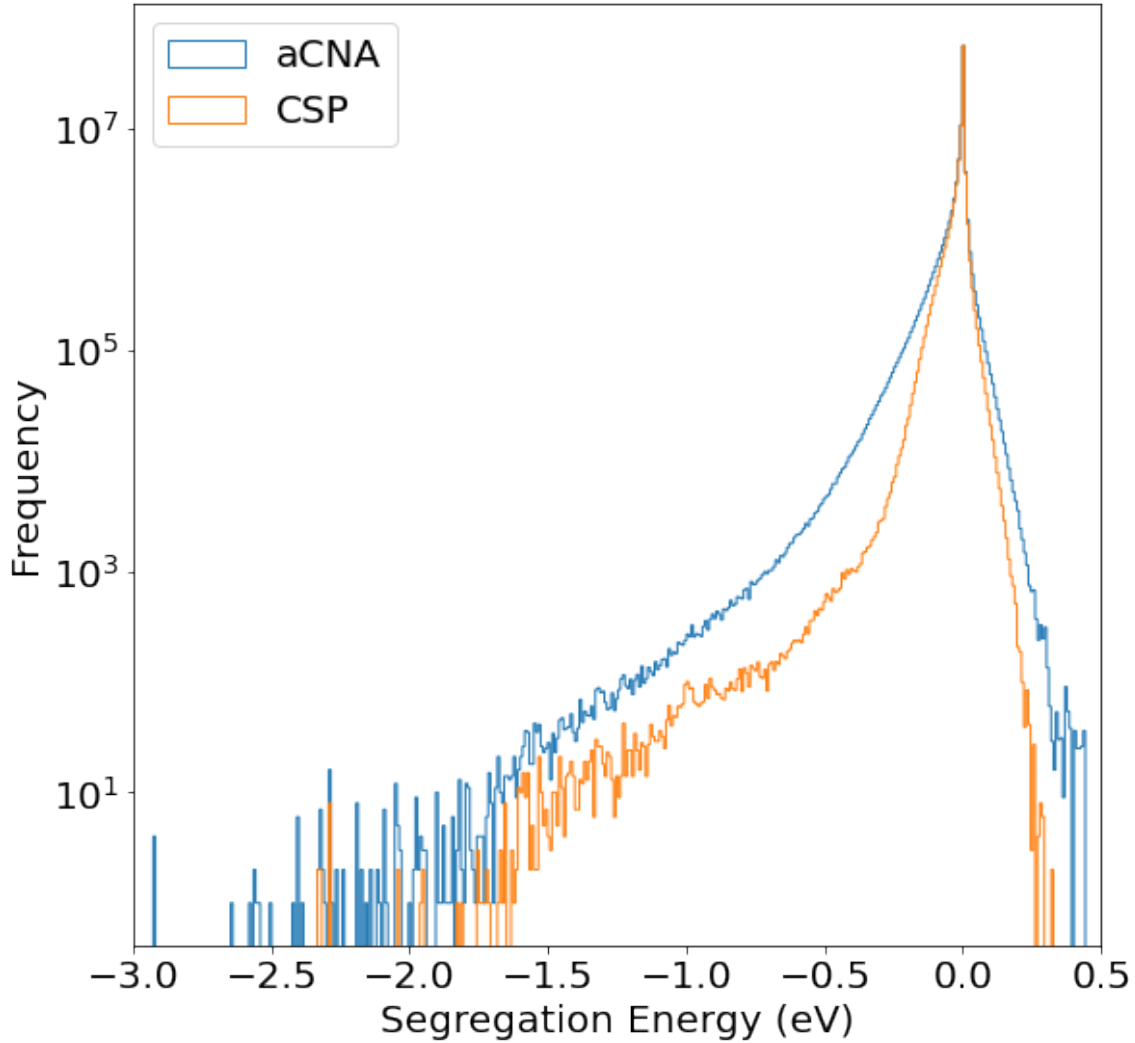
Figure 3.2 Logarithmic scale of the distribution of segregation energies for bulk atoms as determined by CSP ≤ 0.1 (blue) and aCNA (orange). Bin width is 0.008 eV. The aCNA peak is broader because it classifies more distorted atoms as bulk.

relaxation results in almost no change to the atom positions. However, non-negligible changes to the atom positions occur occasionally. The reference energies (E_{Co}^{ref} and E_{Al}^{ref} in Equation 2.1) pertain

to the original pre-substitution configuration and not the restructured configuration, therefore the segregation energy values are not valid when significant restructuring occurs. A valid segregation energy value for the restructured configuration would require calculation of new reference energies.

To determine when GB restructuring occurs and the magnitude of such restructuring, we calculated the mean squared displacement (MSD) for all atoms in a GB during the relaxation following solute substitution. Generally, the MSD at GB atom sites was found to be higher than the MSD at FCC bulk atoms (see Supplemental Figure S7), but there is considerable overlap between the two distributions. A plot of segregation energy vs. MSD is shown in Supplemental Figure S9. In this figure it can be seen that i) the most extreme segregation energies occur when the MSD values are higher and ii) there are also lots of reasonable segregation energies with relatively large MSD values. Here, we examine examples of these two cases.

In one case where the segregation energy was very negative, $E_{\text{seg}}^{\text{Co}_i} = -6.1$ eV, and the MSD value was large, 0.076 Å^2, considerable restructuring occurred during the post-substitution relaxation. To check the accuracy of this atom's segregation energy value, new reference energy values were determined using the restructured GB for the reference energies. The segregation energy value was re-calculated to be $E_{\text{seg}}^{\text{Co}_i} = -0.45$ eV. Restructuring clearly caused the reference energies to be invalid for the post-substitution GB structure in this case, and MSD was a good determination of this invalidity.

In another case where the segregation energy was in the normal range, $E_{\text{seg}}^{\text{Co}_i} = -0.38$ eV, but the MSD was still reasonably large, 3×10^{-4} Å^2, there was minimal restructuring. The accuracy of this atom's segregation energy value was also checked, and even with new reference energy values, the segregation energy value remained the same at $E_{\text{seg}}^{\text{Co}_i} = -0.38$ eV. In this case, the atomic shuffles had no impact on the segregation energy and the larger than expected MSD values were not indicative of invalid segregation energy values.

Although some high MSD value simulations yield valid segregation energies, we attempted to address the issue of invalid segregation energies caused by restructuring by omitting atoms where MSD values were large. We defined a high-MSD cutoff of 10^{-4} Å^2, since it was above this MSD value that the low segregation energies started to diverge (c.f., Supplemental Figure S9). Unfortunately, this approach removed 7 entire GBs and 38% of the atoms from analysis. Additionally, in some individual GBs, most of the data was lost, as illustrated in Supplemental Figure S10, which shows the effect of removing atoms with high MSD values. This approach also removed segregation energy values that were valid, as indicated by the second case examined above. This approach causes severe data loss and could lead to misinterpretations of the results.

Additional analysis showed that most of the extreme (and likely invalid) segregation energy values belonged to a small number of GBs, and these GBs had a high percentage of extreme segregation energy values. In other words, certain GBs were prone to restructuring upon substitution of a solute atom. While not a perfect solution, we removed 18 GBs with segregation energy data less than -3.0 eV, which belong to the population of atoms in the excluded GBs shown in red in Figure 3.3 and listed in Supplemental Table S3. Supplemental Figure S11 shows the segregation energy spectra for other possible segregation energy cutoff values. The chosen cutoff value of -3.0 eV removes most of the extreme values while only removing 0.25% of the GBs simulated.

While this approach leaves some invalid data in the spectrum due to restructuring in individual simulations, the removal of these 18 GBs seemed the best option, as it only removes 0.25% of the GBs. We assume that the contributions of any remaining invalid datapoints to the spectrum is minimal, as illustrated in Figure 3.3. One way to get around this issue in the future would be to recalculate the reference energy values any time restructuring is detected. Unfortunately, recalculating these reference energies after the fact was impractical for this work.

Final dataset

As discussed in Section 3.1, 4 GBs were removed due to the failure to converge to a zero segregation energy value in the bulk. Another 18 GBs were removed from the dataset because they possessed extremely low segregation energy values, as discussed in Section 3.1. There were 10 GBs that were not included due to issues refilling the partially full simulation cells in the dataset. These 32 GBs are listed in Supplemental Table S3. The remaining data contains 70 million atoms with segregation energy values to analyze from 7272 unique GBs. With bulk atoms removed via CSP or aCNA, this number is reduced to 18 or 11.5 million GB atoms, respectively. Despite the imperfections of these methods as discussed above, it is anticipated that this dataset will provide unique insight into segregation energy trends. Having verified the Homer dataset here, we validate it in the following section.

3.2 Validation

In order to validate our work, we compare our results to two computational datasets of Co segregation energies in Al GBs that use the same EAM potential [60] and similar methods to this work; no experimental data for Co enrichment in an Al matrix could be found. Huber et al. examine a number of $\Sigma5$ GBs in [31], and Wagih et al. examine a polycrystal with a variety of different GBs and focus on the overall distribution of segregation energies in [27]. These two datasets are referred to as the Huber dataset and Wagih dataset in the following sections where they are compared with the present results obtained from the Homer dataset.

Comparison to selected $\Sigma5$ GBs

Huber et al. examine solute segregation in a GB dataset of 38 $\Sigma5(53.1°[100])$ GBs [31]. The Homer dataset includes 17 GBs of this type, although the two datasets only have four GBs that share all 5

crystallographic degrees of freedom. Figure 3.4 compares the segregation energy spectra for these four GBs. Figure 3.4a is from the Huber dataset with a kernel density estimation (KDE) fit shown with a solid line and a model fit described in [31] shown with a dashed line. Figure 3.4b is from the present work using the Homer dataset, with segregation energies for non-bulk atoms as determined by aCNA, which is the same method used by Huber et al. [31]. Figure 3.4c is also from the present work using the Homer dataset, but with segregation energies for non-bulk atoms determined by CSP. KDE fits to the distributions in b) and c) are shown with solid lines.

The locations of segregation energy peaks and their relative magnitudes are similar. The $[0\bar{2}1]$ GB has the most favorable comparison, though the Huber dataset in a) has a small scattering of infrequent peaks that do not show up in the aCNA Homer dataset in b). In c), the CSP Homer dataset has an additional peak at approximately -0.05 eV. The $[0\bar{1}2]$ GB has peaks in the same general locations, but slightly different relative magnitudes, again with more scatter in the peaks of the Huber dataset. The CSP Homer dataset again has a large population of atoms with segregation energies near -0.10 eV and an additional peak near 0.10 eV in both b) and c). The $[100]$ GB in our work has a missing peak at approximately -0.55 eV, and an additional missing peak near -0.01 eV in b) that is present in c). Finally, the $[1\bar{1}2]$ GB has more distinct peaks in b) and c) that make up the multimodal distributions around -0.50 eV, 0.00 eV, and 0.30 eV in a), and a higher relative magnitude in the peak near 0.00 eV.

In all of the GBs, c) seems to have more data around -0.05 eV, indicating that bulk determination via CSP leaves a larger population of atoms with near-negligible segregation energies that are removed by the aCNA bulk determination method. This is perhaps why aCNA is used in many other works for bulk classification. However, it can be noted that these values are not identically zero, and contribute to the overall relative frequency of the various peaks. This observation is not to advocate for one method over another, but simply to acknowledge a bias introduced by the method of bulk and GB atom selection.

The segregation energy spectra of the two datasets are in general agreement, with appropriate magnitudes and frequency of occurrence. Clearly there is not an exact match, perhaps due to the GBs not having identical structures or not extracting the same GB atoms. For example, the high symmetry structure of the Σ5 GBs in column 1 of Figure 3.4 has only 6 GB sites as determined by CNA. Any small variations in GB structure and/or GB atom selection could result in the addition or subtraction of a GB atom, which would lead to large changes in the spectra by adding or subtracting entire peaks. For example, the missing peak at approximately -0.55 eV in the $[100]$ GB from the Homer dataset when using both aCNA and CSP indicates that the local atomic environment making up that peak in the Huber dataset is not found in the Homer dataset. With no atomic structures from the Huber dataset published, there is no means to verify this conclusion. However, given the fact that we cannot guarantee identical atomic structures, we consider the general agreement of the segregation energy spectra to be sufficient validation of the Homer dataset in comparison with the Huber dataset.

Comparison to polycrystal spectrum

While the Homer dataset contains only bicrystal GBs, most materials are polycrystalline, containing a GB network with additional features such as triple junctions and facets. Some recent works have focused on extracting segregation energy distributions from polycrystalline simulations [26–29, 50, 51]. Here we compare the spectrum of segregation energies obtained from bicrystals of the present work with that obtained by Wagih et al. from a polycrystal [27]. The Al-Co segregation energy spectrum from the Wagih dataset is represented by a skew-normal distribution of the form:

$$F(E_{\text{seg}}^{\text{Co}_i}) = \frac{1}{\sqrt{2\pi}\sigma} \exp\left[-\frac{\left(E_{\text{seg}}^{\text{Co}_i} - \mu\right)^2}{2\sigma^2}\right] \text{erfc}\left[-\frac{\alpha\left(E_{\text{seg}}^{\text{Co}_i} - \mu\right)}{\sqrt{2}\sigma}\right] \tag{3.1}$$

with the fitted location parameter μ, scale parameter σ, and shape parameter α. Note that these values are not the typical mean, standard deviation, and shape parameter of a normal distribution.[1]

The segregation energy spectra for this work are presented in Figure 3.5. The spectra from the Homer dataset are obtained by combining the individual GB segregation energy spectra from all 7272 GBs. There are two distributions for the two methods by which bulk atoms are removed: aCNA in blue and CSP in orange. The figure includes the Wagih spectrum, scaled to match the two distributions in this work, plotted as dashed black lines, and skew-normal fits in solid lines in corresponding colors to the spectra. Note that the authors use a skew-normal form for the sake of comparison, and did not attempt to find another functional form with a better fit. See Supplemental Figures S5 and S6 for the spectra creating using fixed width bulk determination.

First, we note that the inclusion of bulk-like atoms using the CSP approach leads to a much larger peak near the origin, though other parts of the histogram of segregation energies are very similar between the aCNA and CSP distributions of the Homer dataset. A comparison of statistical measures of the distributions, in the form of Equation 3.1, are provided in Table 3.1. It can be seen from Table 3.1 that the aCNA and CSP distributions of the Homer dataset are in general agreement.

To compare the datasets to the Wagih dataset, we scaled the magnitude of the skew-normal distribution fitted to the Wagih dataset to match the magnitude of both distributions of the Homer dataset. Note that the Wagih dataset uses aCNA for bulk classification. Despite their quantitative and statistical similarity, there are notable differences in the bicrystal and polycrystal spectra. First, in comparison to the polycrystal spectrum, the bicrystal spectrum that uses aCNA has a slightly higher number of sites with segregation energies just greater than zero and a slightly lower number of sites with segregation energies just less than zero. In the inset with the frequency on a logarithmic

---

[1]Others have also observed the skew-normal form of the spectrum of segregation energies in GBs, including when bicrystals are used [74, 75].

Table 3.1 Comparison of skew-normal statistical measures for the distributions shown in Figure 3.5. These parameters—the fitted location parameter μ, scale parameter σ, and shape parameter α—are for the skew-normal distribution described in Equation 3.1. Note that these are not the usual mean, standard deviation, or shape parameter of a Gaussian distribution. Fixed width distributions are shown in Supplemental Figure S5 and Supplemental Table S1.

Dataset	μ	σ	α
Polycrystal [27]	-0.0104	0.3224	-3.300
Bicrystals, no FCC via aCNA	0.0328	0.3794	-2.424
Bicrystals, no FCC via CSP	0.0706	0.3502	-3.365

scale, it can be seen that there is also significant divergence of both bicrystal spectra from the polycrystal spectrum in the lower tail, but this difference is negligible in the linear frequency scale.

The source of the differences in the two spectra is likely due to the differences in the datasets. First, the polycrystal dataset has 16 distinct grains, 72 GBs, and $\sim 10^5$ non-bulk GB atoms [27], in comparison to the 2×7272 distinct grains, 7272 GBs, and $\sim 10^6$ non-bulk GB atoms for the bicrystals in the present work. In addition, the polycrystalline simulation has atomic environments found in GB triple junctions and quadruple nodes that may not appear in bicrystal simulations, or if those environments show up in bicrystal GB simulations, they may appear with a different frequency than they do in a polycrystalline structure.

It has been shown that small populations of bicrystal GBs fail to produce the same segregation energy distributions as those of polycrystalline materials [50, 51], but that as the population diversity increases with GBs of lower symmetry, there is better coverage of the atomic environment space [51]. The present dataset of 7272 bicrystal GBs is comprised of mostly low symmetry GBs; only 89 of the 7272 grain boundaries, or 1.2%, have low CSL values (i.e., $\Sigma \leq 10$), suggesting that issues related to diversity in the dataset are minimized by the large variety of GBs in the Homer dataset.

Conversely, the polycrystal simulation with its 72 GBs may not provide adequate sampling of the variation in structure across the 5D space, or be large enough to be considered a representative volume element (RVE) such that it is truly representative of atomic environments in a polycrystal. The Mackenzie Distribution, which represents the distribution of disorientation angles for a polycrystalline sample with random cubic crystal orientations [76, 77], can be used as a justification for the selection of an RVE [78]. As shown in Figure 3 of [57], the Homer bicrystal dataset gives a reasonable approximation of the Mackenzie Distribution. The Wagih polycrystal dataset does not claim to follow the Mackenzie Distribution of disorientations, nor do they consider their simulation to be an RVE. Wagih et al. do however assert that their simulations are similar enough to randomly oriented grains to represent the local atomic environments present in the polycrystalline GB space, and that the segregation energy spectrum obtained is universal to any segregation energy spectrum obtained from a polycrystal [26, 51].

At this point, it is unclear if the differences between the Wagih and aCNA bicrystal distributions are significant. The degree to which either of the methods incorporates aspects of the distribution of GBs that are critical to a proper representation of segregation energies in a diverse polycrystal is also unclear. The discussion leads to several unanswered questions:

1. How many GB types would be needed to establish an RVE for segregation energies? (i.e., is the polycrystal sample from Wagih et al. large enough? Does the present work have enough and sufficiently diverse bicrystals to represent a polycrystal?)

2. How would a change in GB texture of the polycrystal change the GB sampling and thus the segregation energy spectrum? (i.e., does the texture used in the work of Wagih et al. bias the sampled spectrum significantly? Is it appropriate to make these distributions from a random sampling?)

3. To what degree do the local atomic environments of triple junctions and quadruple nodes affect the sampled segregation energy spectrum? (i.e., the volume fraction of such atomic environments will be different in nanometer-sized grains as compared with micron-sized grains, and may be entirely absent from the bicrystal dataset of this work.)

We leave these questions to the community to address. Nevertheless, the similarity in the two spectra is seen as a positive validation of the methods and use of the Homer GB dataset in this work.
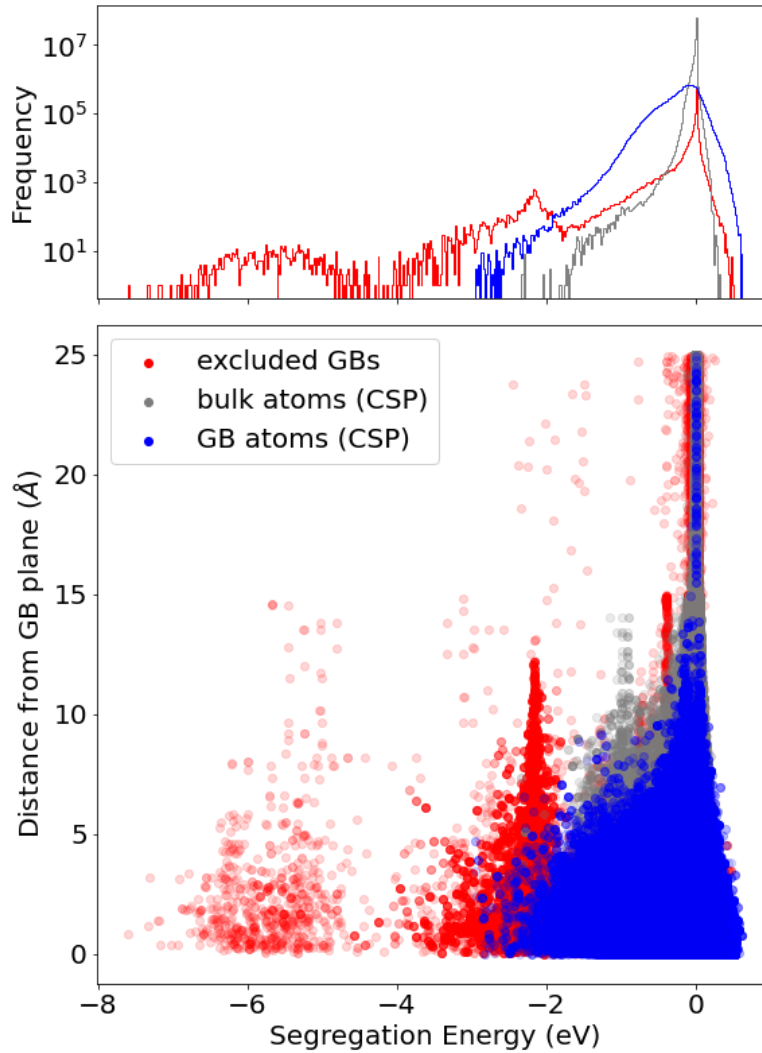
Figure 3.3 (Top) Histograms of segregation energy for GB atoms (blue), bulk atoms (gray), and atoms in GBs excluded due to invalid calculations (red). Bin width is 0.165 eV. A linear-scale histogram with the same data is included as Supplemental Figure S8 to show how low segregation energies contribute negligibly to the distribution. (Bottom) Distance from the GB plane in Å as a function of segregation energy, ($E_{\text{seg}}^{\text{Co}_i}$). In the GB construction simulations, the GB plane is initialized at $z = 0$ Å and is allowed to shift as the simulation cell relaxes, however, this distance is calculated as a distance from $z = 0$ Å. The non-converged and low energy GBs that were removed from analysis as described in Sections 3.1 and 3.1 are shown in red, the bulk FCC atoms as determined by a CSP cutoff of 0.1 are shown in grey, and the non-bulk GB atoms are shown in blue. The distribution decays to 0 eV as the distance from the GB increases (with the exception of the excluded GBs, shown in red), as predicted in [62, 63].
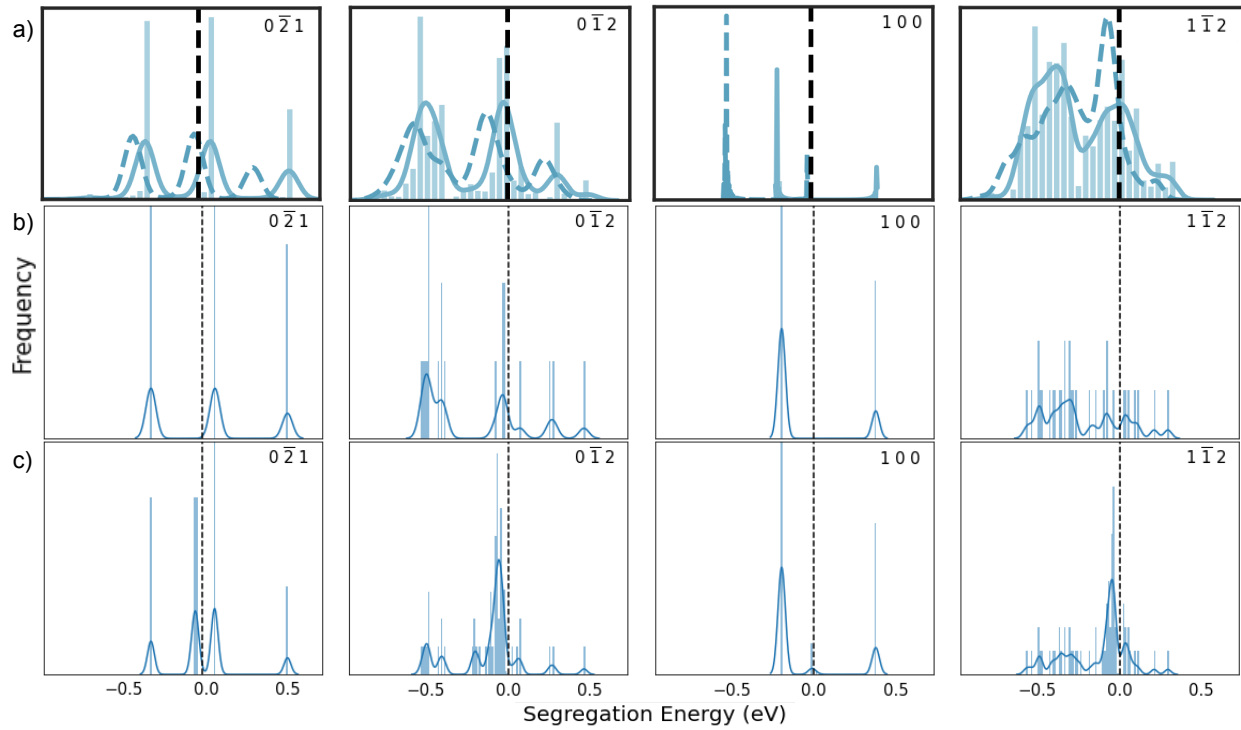
Figure 3.4 Segregation energy distributions of the shared Σ5 GBs between the a) Huber dataset from [31] (bin width 0.04 eV) and the b/c) Homer dataset (bin width 0.01 eV). a) has two fit lines: a KDE fit to the data (solid) and a model fit discussed in [31] (dashed). b) includes the non-bulk atoms from this work as determined by aCNA (the same method of FCC atom removal as is used in [31]). c) includes the non-bulk atoms from this work as determined by CSP. The Huber dataset in a) is reproduced from [31] and relabeled according to the Homer dataset labelling conventions [52].
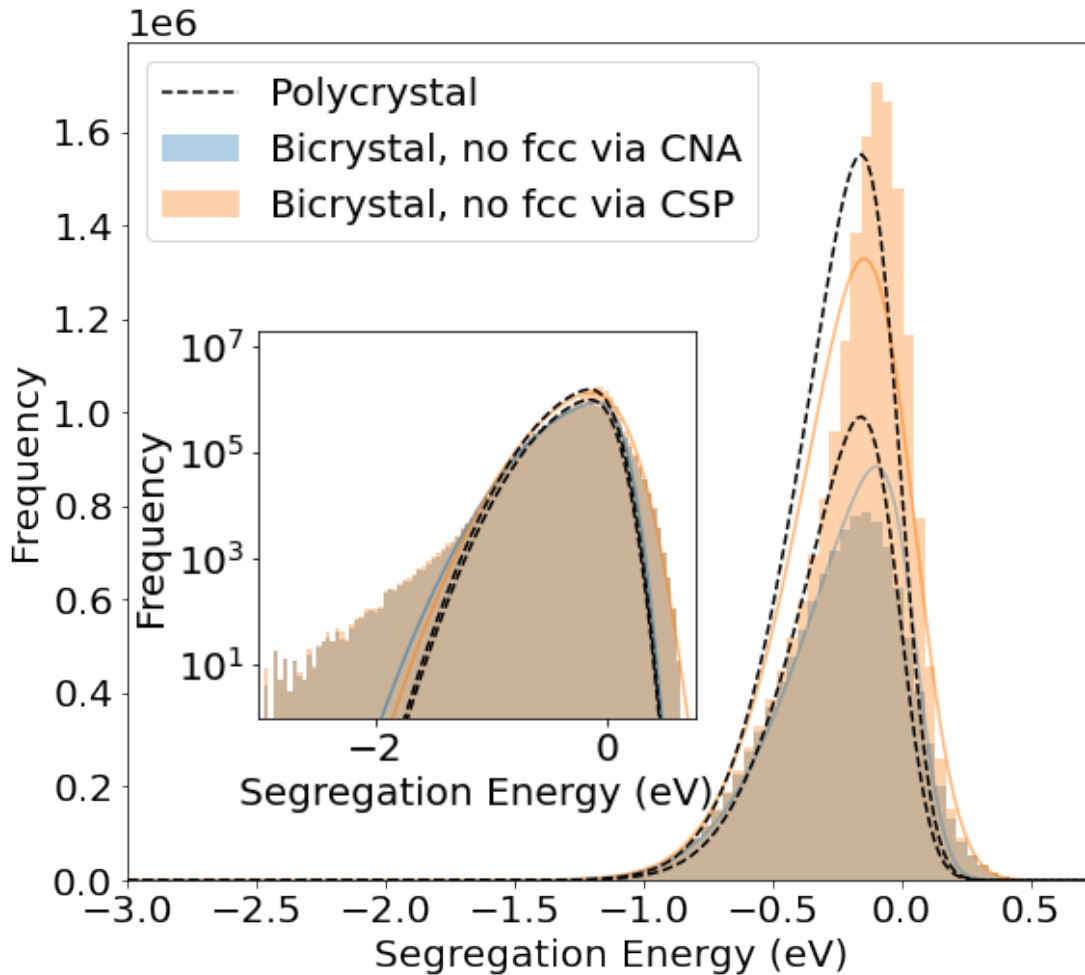
Figure 3.5 The spectrum of segregation energies aggregated from all GBs simulated in this work, with all bulk atoms removed via aCNA (blue) and via CSP (orange), with fit lines for their respective skew-normal distributions in the form of Equation 3.1 in their respective colors. The dashed black lines are the polycrystal spectrum from Wagih et al. in [27], scaled to both of this work's distributions. Inset are the same spectra on a logarithmic scale. Statistics for each skew-normal distribution are given in Table 3.1. The spectrum of all atoms (including bulk atoms) is shown in Supplemental Figure S12. Bin width is 0.0412 eV.

Chapter 4

Results & Discussion

Having provided some context and discussion of the results in the Verification and Validation section, we begin our analysis here by taking several different views of the segregation energy spectra produced in this work. Note that most of the results presented in this section are produced using CSP to determine bulk atoms, but similar results would be obtained using aCNA, as shown in the supplemental materials and described in Section 4.4.

Examining the spectra of segregation energies across the 5D space is challenging because at each point in the space we obtain a spectrum of segregation energies. To provide insight into the dataset, we employ several different tactics: i) statistical measures of the spectra, ii) classification of the segregation energy spectra into fractions of atoms segregating, anti-segregating and negligibly segregating, and iii) calculation of a GB solute concentration for each GB (c_{GB} defined in Equation 2.2) based on Coghlan and White's model [22]. Each of these provide different insight into trends in the large set of GBs.

Table 4.1 Statistics for the Σ5 GBs shown in Figure 3.4. Note that the the max, mean, and min values in the table refer to the maximum, mean, and minimum values from each GB's $E_{\text{seg}}^{\text{Co}_i}$ spectrum.

GB	max (eV)	mean (eV)	min (eV)	f_{seg}	f_{negl}	f_{anti}	c_{GB} (at.%)	$\gamma\left(\frac{\text{mJ}}{\text{m}^2}\right)$	$V_{\text{exc}}\left(\frac{\text{Å}^3}{\text{Å}^2}\right)$
$0\bar{2}1$	0.52	-0.01	-0.31	0.29	0.29	0.43	28.9	494	0.529
$0\bar{1}2$	0.46	-0.14	-0.53	0.47	0.40	0.14	37.7	496	0.347
100	0.34	-0.05	-0.20	0.44	0.44	0.11	35.5	326	0.296
$1\bar{1}2$	0.30	-0.18	-0.57	0.58	0.24	0.18	59.7	472	0.340

4.1   Statistical measures of the spectra

In this section, to examine the segregation energy spectra across all of the dataset, we present the mean, maximum, and minimum values of the multimodal distributions of each GB's segregation energy spectrum. As an example, the maximum, mean, and minimum values for the Σ5 GB spectra shown in Figure 3.4c are given in Table 4.1.

Although this represents a significant reduction of information, some observations can be still made by comparing these values against one-dimensional parameterizations of the GB dataset. For example, these values are plotted as a function of GB interface energy, γ, in Figure 4.1 and disorientation angle in Supplemental Figure S13. Generally, the mean segregation energy of a GB becomes more negative as GB energy increases, as shown by the green datapoints and trendline in Figure 4.1. Note that the [111] symmetric twist GBs (aside from the lowest energy perfect twin GB) have a slight increase of the mean segregation energy as GB energy increases, contrary to the general trend. We will further analyze this subset of GBs in Section 4.3 because of their likely presence in Al [79]. The average range of segregation energies also increases as a function of GB energy, as indicated by the linear fits to the three populations shown in black. This is probably due to greater deviation from the bulk FCC structure in the higher energy GBs, which likely leads to a

greater distribution of segregation energies in the solute atom sites. Finally, it can be seen in Figure 4.1 that the lower the mean segregation energy for a GB, the higher the probability for segregation in that GB.

GB energy, γ, has been shown to have a Read-Shockley relationship with disorientation angle [80, 81]. Despite the relationship observed between GB energy and mean segregation energy, there is no observable transitive relationship between mean segregation energy and disorientation angle (see Supplemental Figure S13). It is interesting that the two separate correlations do not result in the correlation between segregation energy and disorientation angle. While the correlation of segregation energy with GB energy provides some insight to global trends in segregation energy, we continue with more detailed analyses of the dataset.

4.2 Classification of the spectra

To examine the segregation energy spectra in this section, we employ the segregation energy classifications described in Section 2.3. This approach classifies each atom based on its segregation energy value into one of three categories: i) segregating ($E_{\text{seg}}^{\text{Co}_i} < -0.0875$ eV), ii) negligibly segregating (-0.0875 eV $\leq E_{\text{seg}}^{\text{Co}_i} < +0.018$ eV), or iii) anti-segregating ($E_{\text{seg}}^{\text{Co}_i} \geq +0.018$ eV). Using these classifications, we compute the fraction of atoms in each GB that fall into each category, i) f_{seg}, ii) f_{negl}, and iii) f_{anti}. For each GB, these fractions add to 1 (i.e., $f_{\text{seg}} + f_{\text{negl}} + f_{\text{anti}} = 1$). As an example, the f_{seg}, f_{negl}, and f_{anti} values for the $\Sigma5$ GB spectra shown in Figure 3.4c are given in Table 4.1.

The distributions of these fractions for the 7272 GBs are shown in Figure 4.2a; these are the distributions for non-bulk atoms identified using the CSP scheme. The mean value for these categories over all GBs are $\overline{f_{\text{seg}}} = 0.62$, $\overline{f_{\text{anti}}} = 0.15$, and $\overline{f_{\text{negl}}} = 0.23$, as shown by the dotted vertical lines in Figure 4.2a. The global fractions in the aggregated spectrum are $f_{\text{seg}} = 0.63$, $f_{\text{anti}} = 0.15$, and $f_{\text{negl}} = 0.22$.

In Figure 4.2b, this same data is shown on a ternary plot, that shows the 2D plane that the 3D points all lie on, since they all add to 1 (i.e., $f_{seg} + f_{negl} + f_{anti} = 1$). The data points in the plot are colored by GB energy, γ. It can be seen in Figure 4.2b that increased GB energy corresponds to an increased fraction of segregating atoms, f_{seg}. This supports the trend for more negative segregation energies with higher GB energy observed in Figure 4.1. To see the same plots for aCNA, see Supplemental Figure S14.

As expected from the histograms, the general distribution of points in Figure 4.2b is located closest to the "all segregating" corner of the triangle. There are several notable outliers. The [111] perfect twin GB is located at "all anti-segregating", and its closest neighbor in the ternary plot has the same misorientation of $60°$ about the [111] axis. [100], [110] and [111] disorientation axis GBs make up 50% of the GBs along and near the top right edge of the triangle with $f_{negl} \leq .1$. 34% of the GBs with $f_{anti} \leq .075$ belong to the [111] disorientation axis.[1] Thus, many of the outliers in the ternary plot belong to high symmetry disorientation axes. Additionally, it can be seen that there are a number of GBs along the left side of the plot which have no anti-segregating atoms, though this is perhaps unsurprising given the proximity of the distribution to this edge and the tendency to segregate in this system.

In short, most GBs have a tendency to segregate, evidenced by the $\overline{f_{seg}}$ value of 0.62. Additionally, high energy GBs have a tendency to segregate more than lower energy GBs, which is supported by the results shown in Figure 4.1. However, while these trends are interesting, this analysis is still insufficient to predict segregation behavior generally.

---

[1]To see the ternary plot with the [111] disorientation axis GBs highlighted, see Supplemental Figure S15.

4.3   Solute concentration at GBs

One of the challenges with the representations of the segregation energy spectra analyzed in the preceding sections is that they still have multiple values for each GB, which makes it hard to analyze trends across the 5D space. As such, we have included the calculation of the grain boundary solute concentration, c_{GB}, from Equation 2.2. This singular value for each GB allows the display of some trends more clearly in subsets of the 5D space that still take into account attributes of the full spectrum of GB energies, as the value is computed from a sum over the whole spectrum of GB atoms in each GB. Note that most of the c_{GB} values presented in this section are well above the dilute limit; as such, many of the assumptions made in the calculation of the concentration values (e.g., neglecting solute-solute interactions) are invalid. However, we assume that the general trends observed in c_{GB} are still valid.

As with the other sections, the c_{GB} values for the $\Sigma5$ GB spectra shown in Figure 3.4c are given in Table 4.1. However, because c_{GB} takes into account the full spectrum, we use a set of GBs that have a unique trajectory through the 5D space of GB crystallographic character to illustrate the c_{GB} values. This set of GBs is the low GB energy [111] symmetric twist GBs noted in [57] and mentioned in Section 4.1, used because they have a large range of disorientation angles, their likely appearance in Al due to their low energy [79], and because they show interesting segregation energy results. However, care should be exercised in extrapolating the [111] symmetric twist GB results to rest of the dataset precisely because they are low energy GBs and may behave differently. Note that the disorientation angles related to these particular boundaries also define their twist angles about the [111] axis.

The [111] symmetric twist GBs exhibit an energy trend of an inverted parabola with low GB energy values at low and high disorientation angles, illustrated in blue in Figure 4.3a. A corresponding trend for GB excess volume is also shown in orange in Figure 4.3a. Figure 4.3b plots the segregation energy spectra for the GB atoms as determined by aCNA (blue) and CSP (orange)

for each of these GBs, against their disorientation angle. Note the data loss from using aCNA (blue) over CSP (orange), which was discussed in Section 3.1. Also note the exclusion of many near-bulk segregation energies in the CSP (orange) spectrum.

Although a significant portion of each GB's spectra falls in the "negligible segregation" category shown by horizontal dotted black lines in Figure 4.3b, a majority do not, and almost all of the non-negligible segregation energies are negative, implying that a Co atom added to an Al [111] symmetric twist GB will prefer to segregate to the GB. With the exception of the perfect twin, this segregation data shown in Figure 4.3b generally runs counter to the general trend that was observed in Figure 4.1 for lower energy GBs to have less segregation than higher energy GBs. This is evidenced by the more negative segregation energy spectra in Figure 4.3b for the corresponding lower GB energies in Figure 4.3a, and was perhaps expected from the analysis of the [111] symmetric twist GBs shown with black "x" markings in Figure 4.1.

In Figure 4.3c, we show the c_{GB} values as determined by CSP (solid) and aCNA (dotted) for the [111] symmetric twist GBs as a function of disorientation angle at 3 different temperatures. In addition to the low energy GBs in this dataset having more negative segregation energies, they also have higher solute concentrations, excepting the perfect twin at $60°$. This is seen most clearly in the c_{GB} line for 300 K (orange) in Figure 4.3c. This correlation is expected from the inverse relationship between segregation energy, $E_{\text{seg}}^{\text{Co}_i}$, and solute concentration, c_{GB}, in Equation 2.2, and can be seen clearly by the paraboloid quality of the segregation energy spectra across disorientation angles in Figure 4.3b with a matching inverse paraboloid in Figure 4.3c.

As demonstrated in Figure 4.3c and expected from Equation 2.2, the concentration of solute at the GB, c_{GB}, is temperature dependent. Note that segregation energies were calculated at 0 K, but that Equation 2.2 expects this to be the case. We expect that as the temperature increases, less favorable atom sites in the bulk of the material are occupied with increasing probability. This causes the concentration to approach the bulk value of $c_{\text{bulk}} = 0.2$ at.% at elevated temperatures, which is

shown clearly by the decreasing concentration values at higher temperatures in Figure 4.3c. Thus the concentrations calculated here match the theory presented in Section 2.3.

The perfect twin GB at a 60° twist angle about the [111] disorientation axis is an exception to most of the trends in the [111] symmetric twist GBs discussed here. For example, it has all positive segregation energies, shown in Figure 4.3b. This is unsurprising given the structure of the twin boundary; its density and structure provide no easy sites for segregation as compared with the bulk (evidenced by its low excess volume), leading to positive segregation energy values in all cases. The highly symmetric structure also results in a very low GB energy, shown in Figure 4.3a. The perfect twin has lower c_{GB} values than the rest of the [111] symmetric twist GBs at every temperature, as shown in Figure 4.3c, as a result of its entirely positive segregation energy spectrum. It is also the only GB in the Homer dataset with a c_{GB} value below $c_{bulk} = 0.2$ at.%, having a value of $c_{GB} = 0.03$ at.% for $T = 300$K.

It can be seen that aCNA and CSP give similar results at 300 K (compare the 300 K solid and dotted lines in Figure 4.3c). This was found to be the case for the entire dataset; the correlation between c_{GB} computed from CSP vs. aCNA GB atoms is plotted in Supplemental Figure S16. Using CSP nearly always results in a similar, but slightly lower, c_{GB} value since it includes more near-bulk atoms than aCNA, but the positive correlation means that all trends should remain the same. This similarity in c_{GB} emerges despite the differences in the distributions shown in Figure 4.3b), though it is difficult to point to specific aspects of the distributions that lead to bigger differences in c_{GB} based on CSP and aCNA for some GBs than others.

Having examined the [111] symmetric twist GBs, we now turn our attention to the c_{GB} values for all 7272 GBs over the 5D space. 82.1% of non-FCC GB atom sites observed in this work, as determined by CSP, have negative segregation energies, which corresponds to segregation being favorable. Therefore, a majority of GB sites will accommodate a Co atom in the dilute limit. This implies that the concentration of Co atoms in the GB, c_{GB}, will be higher than in bulk value of

Table 4.2 Disorientation axes with the highest mean c_{GB} values, and the number of GBs that belong to that axis.

Disorientation Axis	$\overline{c_{GB}}$ for this axis	# of GBs
[443]	52.7 ± 4.6 at.%	86
[751]	51.4 ± 5.5 at.%	108
[654]	51.3 ± 7.7 at.%	20

Table 4.3 Disorientation axes with the lowest mean c_{GB} values, and the number of GBs that belong to that axis.

Disorientation Axis	$\overline{c_{GB}}$ for this axis	# of GBs
[100]	40.6 ± 6.7 at.%	217
[554]	41.1 ± 8.5 at.%	32
[110]	42.6 ± 10.4 at.%	352
[111]	43.0 ± 11.6 at.%	253

$c_{bulk} = 0.2$ at.%, and is evidenced by the mean concentration of all GBs in the Homer dataset, which is $\overline{c_{GB}} = 46.7 \pm 7.2$ at.% at $T = 300$K. Supplemental Figure S17 shows c_{GB} vs. GB energy for all GBs in the Homer dataset. Supplemental Figure S18 shows c_{GB} as a function of disorientation angle.

The disorientation axes with the highest and lowest mean c_{GB} values are given in Tables 4.2 and 4.3, respectively. It is worth noting that the low c_{GB} disorientation axes in Table 4.3 have high symmetry, with the exception of the [554] axis. However, it is also worth noting that the mean c_{GB} for the entire dataset lies within one standard deviation of each of both the low and high concentration disorientation axes' mean values given in Tables 4.2 & 4.3, aside from the [443] axis. Thus, there is considerable overlap in the distributions. Additionally some of the axes listed here may not be statistically significant enough to be considered outliers, based on their small populations

(e.g., the [654] GB containing only 20 GBs). So, while they may have more extreme c_{GB} values in general and also contain some of the GBs with outlying ternary plot locations mentioned in Section 4.2, the actual range of c_{GB} values in all cases is not large and it is difficult to find meaningful trends among the averaged values of the disorientation axes.

The effect of disorientation is shown in Supplemental Figure S20, where the mean concentrations of all of the Homer dataset GBs at each CSL are plotted in Rodriguez space.[2] Consistent with Table 4.3, the [100], [110], and [111] disorientation axis GBs have the lowest $\overline{c_{GB}}$ values per disorientation axis, although the [111] axis has a larger deviation. The smooth variation of c_{GB} in Rodriguez space is an indicator that there may be broader global trends in c_{GB}, but because these represent averages of dozens of c_{GB} values for the different boundary planes, any functional would be complex.

The effect of boundary plane is illustrated in Figure 4.4, which shows three small subsections of the 5D GB space—the a)[100], b)[110], and c)[111] disorientation axis GBs. Shown are volumetric plots of concentration, c_{GB}, where the z-axis defines the disorientation angle and the x- and y-axes define a stereographic projection of the boundary plane normal in boundary plane fundamental zones. The vertices of the plots define high symmetry boundaries; the two vertices that terminate each arc are symmetric tilt boundaries about the disorientation axis and the other vertex defines symmetric twist boundaries about the disorientation axis. The [111] symmetric twist boundaries examined in Figure 4.3 correspond to the points along the red line in Figure 4.4c.

All three plots in Figure 4.4 show smooth but unpredictable variation of the c_{GB} from areas with high c_{GB} to other areas of low c_{GB}. We refer to this as a complex or rugged landscape [82]. This means that while c_{GB} varies smoothly, there are many irregular local extrema and a lack of symmetry or global trends. Of the three axes shown in Figure 4.4, the c) [111] disorientation axis exhibits the largest range of c_{GB}. This is perhaps unsurprising because it has the low energy twin

---

[2]Rodriguez space is also known as Rodriguez-Frank space and is a fundamental zone where the CSL values of cubic-cubic disorientation GBs are defined. It is a 3D parameterization of disorientation, and as such is often used to aid in visualization of 5D datasets of GBs.

GB at the top of the red line, and Table 4.3 shows that it has a large standard deviation of 11.6 at.%. Additionally, as noted above, GBs from the three axes in Figure 4.4 make up many of the outliers in the ternary plot in Figure 4.2b, which may be related to their low mean c_{GB} values (noted in Table 4.3) as compared to the global mean concentration of $\overline{c_{GB}} = 46.7$ at.%. However, as stated earlier, not every GB from these axes will be an outlier.

While there are not broad global trends that we can extract from these few subspaces analyzed, these plots illustrate the effects of disorientation and boundary plane on changes to segregation energy spectra in grain boundaries. The segregation energy spectra or c_{GB} values computed in this work could be used to develop a model for segregation across the 5D space (e.g., using an expansion [83] or an interpolation function [84]). Such a model could subsequently be used to examine the effects of texture or estimate segregation for a GB of arbitrary character.

4.4 Overall trends in dataset

The broad effect of GB crystallographic character on GB segregation trends has to this point been unknown and was recently listed as a future perspective worth considering [48]. The plots of c_{GB} in Figure 4.4 and Supplemental Figure S19 show that segregation varies smoothly throughout the 5D crystallographic space. Unfortunately, the landscape produced in this work is rugged and beyond the averaged trends observed in the Rodriguez plot in Supplemental Figure S20, there is no obvious global trends of segregation as a function of 5D crystallographic character. This is futher illustrated in Figure 4.5, where the scatter in the data makes it hard to observe any obvious trend.

This stands in contrast to a variety of experimental reports that show trends of grain boundary enrichment as a function of misorientation angle [20, 43, 63, 85]. While these various reports do consistently show different results for low vs. high angle GBs, the trends at high angles are highly variable between the different reports, which could be attributed to the comparison of different

materials or different sets of GB types. Finally, most involve small samplings of GBs, likely due to the difficulty in experimental measuring GB enrichment in a large population of GBs.

It is not clear at this point whether the various sources of information are in conflict or in support of the results presented here. It is certain that at least some of the differences between the reports should be attributed to different materials, structures, and their segregation tendencies. But the variation due to GB type could be the sign that there are local but not global trends in GB concentration as indicated by the present work. Additional experiments will be required to verify whether their limited data is representative of broader global trends or whether they have extracted local trends.

To determine whether we have missed a possible global low vs. high angle GB characterization often reported in the literature, we fit GB concentration as a function of disorientation angle for GBs with angles less than 15°. These fits are provided in Supplemental Figure S18 where it can be seen that R^2 values for the low angle fits are all less than 0.3. This is insufficient to verify a global low vs. high angle trend, so once again, it may be that there are local but not global trends even in this simplified characterization. The slightly better fit in the fixed width GB atom selection once again highlights the need to further understand the effect of GB atom selection. More importantly, more low angle data would be required to definitively say that the computational data does or does not match the experimental observations; only 6 unique misorientations over 250 boundary planes exist in the Al dataset.

However, given that c_{GB} and the segregation energy spectrum do appear to correlate with GB energy and GB excess volume at the local scale, as illustrated in this work by the [111] symmetric twist GBs in Figure 4.3 and by others [27, 56, 65, 85–87], we examine these correlations further. In addition, segregation energies appear to be correlated with GB energy across the whole dataset as illustrated in Figure 4.1. This is supported by observations from Huber et al. in their exploration of

Table 4.4 Estimate, standard error (SE), and *p*-value of variables of the following linear model used to predict c_{GB} in at.%: $c_{GB} = x_0 + x_1 \cdot \gamma + x_2 \cdot V_{exc} + x_3 \cdot \theta_{dis}$.

Variable	Estimate	SE	$p-$value
x_0	7.08	0.496	1.33×10^{-45}
x_1	0.175	0.00154	0
x_2	-142	1.63	0
x_3	0.00504	0.00410	0.220

Σ5 GBs, who found that segregation energy per site depended on excess volume and coordination number at the site.

Given these apparent correlations, we created a simple linear model to predict c_{GB}. We include disorientation angle to search for possible crystallographic dependence as well as two variables known to correlate with segregation, GB energy and GB excess volume. A plot of these variables, excluding disorientation angle, is shown in Figure 4.6. The linear model is given in Table 4.4. The model has an R^2 value of 0.642 and a root mean squared error (RMSE) value of 0.043 at.%. In contrast, a linear model of c_{GB} as a function of GB energy alone, shown in Supplemental Figure S7, has an R^2 value of 0.271. A plot of c_{GB} vs. disorientation angle is shown in Supplemental Figure S18 to confirm the lack of a global correlation with θ_{dis} found in the model; the p-value on the coefficient is 0.217.

Figure 4.6 and the linear model given in Table 4.4 confirm the previously shown dependence of segregation on GB energy, γ, and GB excess volume, V_{exc}, for GBs sampled over the entire 5D space. However, the linear model for c_{GB} has almost no dependence on the disorientation angle, θ_{dis}.

This lack of a relationship with the disorientation angle as well as the rugged landscape in 5D space shown in Figure 4.4 make it difficult to understand how to optimize GB segregation energy characteristics through texture control or GB engineering. It may be that sufficient advantage can be

obtained through traditional GB engineering efforts to obtain large populations of low-angle GBs or Σ3 and other special CSL GBs to obtain enhanced properties, as in [43, 53, 85]. GB engineering for segregation through the use of other types of boundaries remains a challenge to be solved.
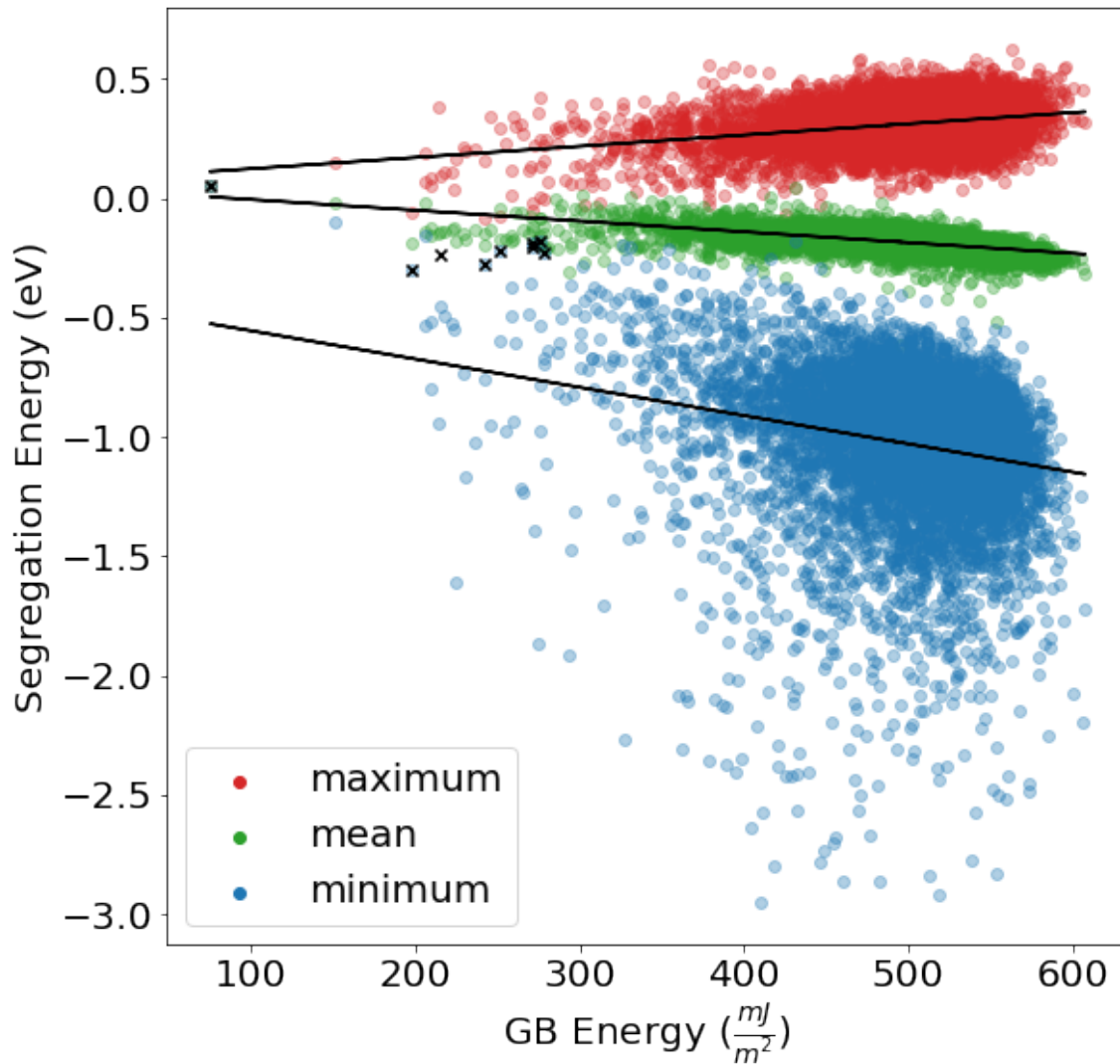
Figure 4.1 Maximum (red), mean (green), and minimum (blue) values of the segregation energy, $E_{\text{seg}}^{\text{Co}_i}$, spectrum for each GB vs. their GB interface energy, γ. Linear fits for each are shown in black. The mean segregation energy for the [111] symmetric twist GBs are shown with black "x" markings. The range of segregation energies increases with GB energy, and the mean segregation energy has an inverse relationship with increasing GB energy.
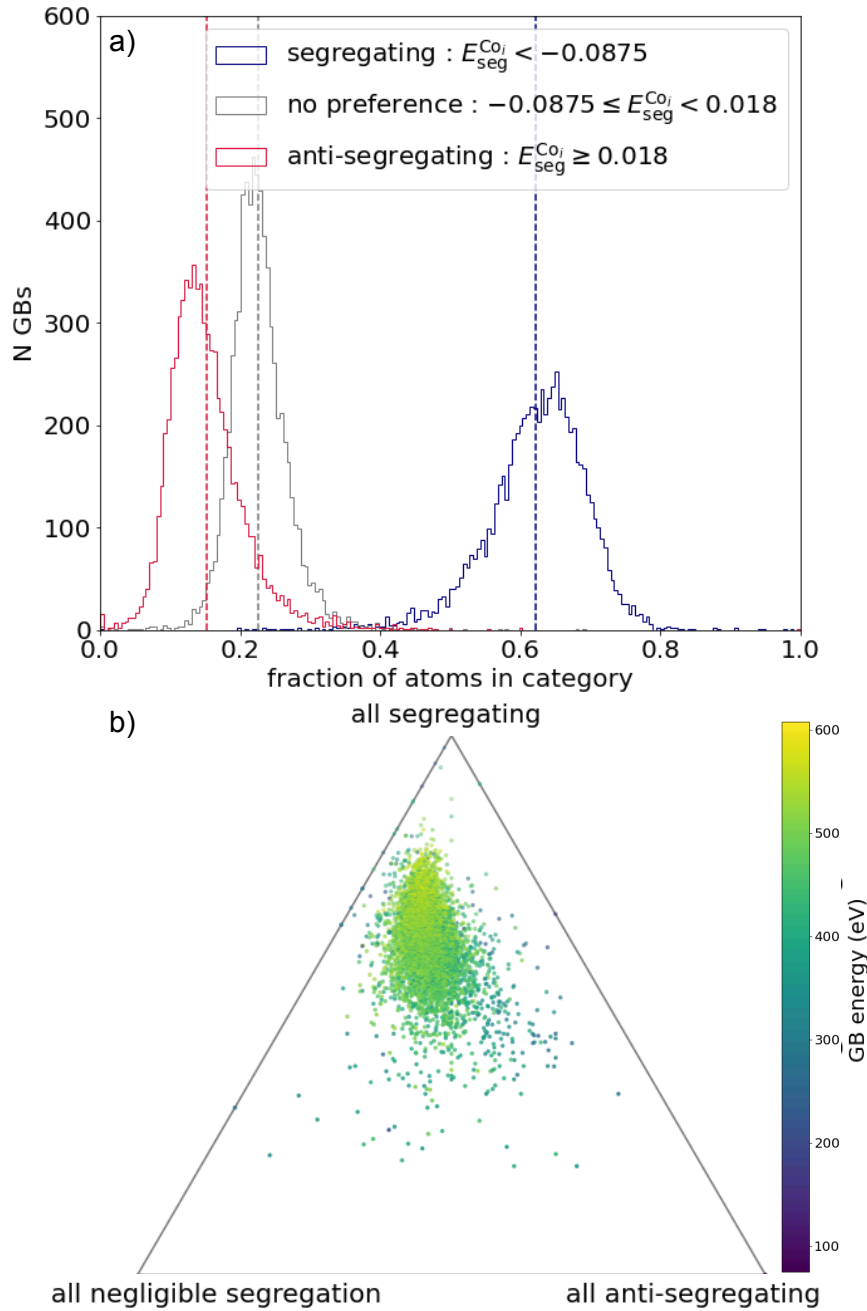
Figure 4.2 a) Histograms of f_{seg} (blue), f_{anti} (red), f_{negl} (grey) for GB atoms as determined by CSP. The mean of each histogram is marked with a dashed vertical line of a corresponding color. Bin size is 0.005 eV. b) Ternary scatter plot of the same data, colored by GB energy, γ. Since the sum of these values is 1 (i.e., $f_{seg} + f_{anti} + f_{negl} = 1$), they lie on a 2D plane in 3D space.
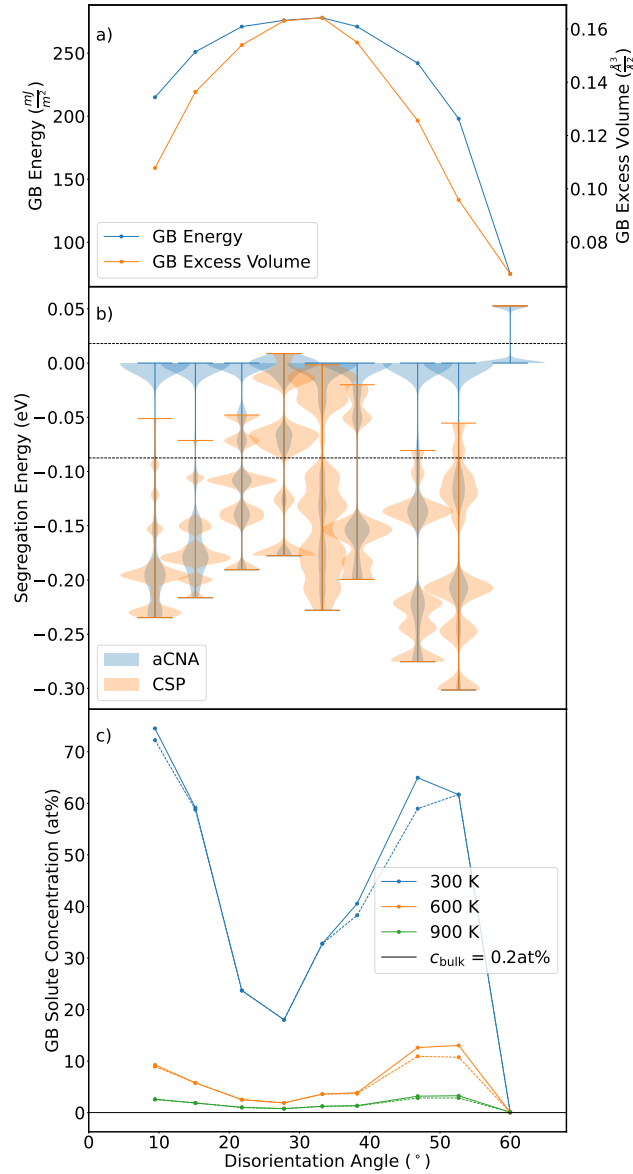
Figure 4.3 a) Plot of GB energy ($\frac{mJ}{m^2}$) and GB excess volume ($\frac{\mathring{A}^3}{\mathring{A}^2}$) as functions of disorientation angle (°) for the [111] symmetric twist GBs. b) Plot of the segregation energy (eV) spectra for GB atoms as determined by CSP (orange) and aCNA (blue) in the [111] symmetric twist GBs, against their disorientation angles. Aside from the perfect twin GB at 60° twist, their segregation energies are almost always negative, or favorable to segregation. The "negligible segregation" (-0.0875 eV $\leq E_{\text{seg}}^{\text{Co}_i} < +0.018$ eV) limits are shown with dotted black lines. c) Concentration of solute at the GB, c_{GB} (at.%), as a function of disorientation angle (°) and temperature for the [111] symmetric twist GBs, for CSP (solid) and aCNA (dotted). This is calculated using Equation 2.2. The bulk concentration, $c_{\text{bulk}} = 0.2$ at.%, is shown with a solid black line.
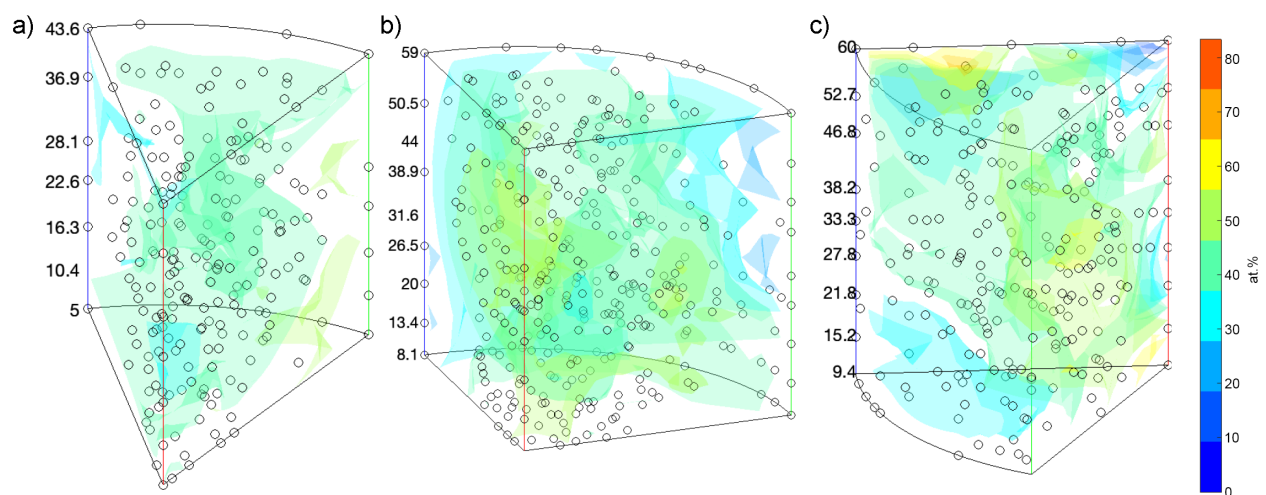
Figure 4.4 Disorientation angle vs. boundary plane volumetric plots of concentration in the GB, c_{GB}, with isosurfaces colored by different c_{GB} values for 3 different disorientation axes: a) [100] b) [110] c) [111]. These plots are equivalent to stacking boundary plane fundamental zone plots with the same disorientation axes. The [111] symmetric twist GBs are located along the vertical red line in plot c), with the perfect twin located at the top, corresponding to the darkest blue contour, and the lowest c_{GB}.
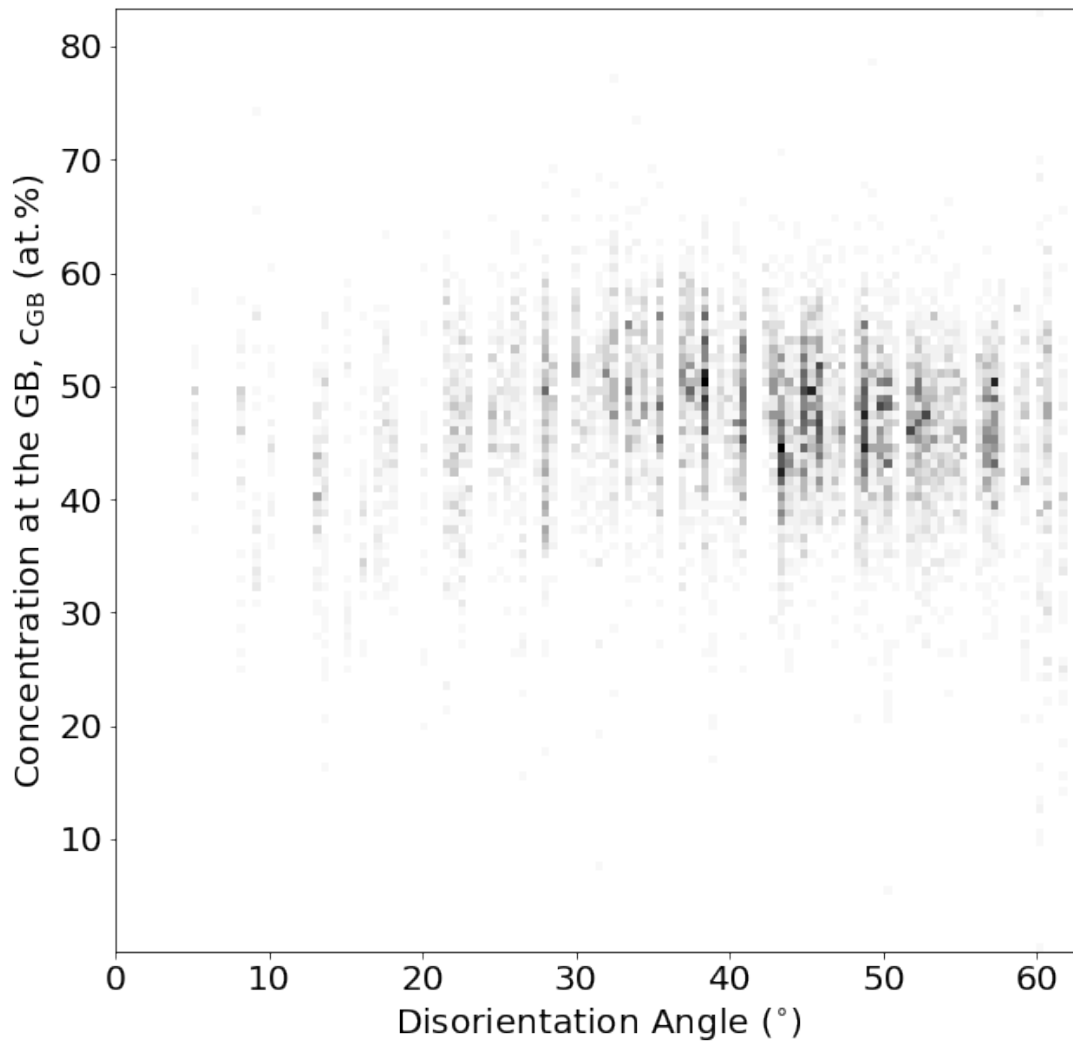
Figure 4.5 Disorientation angle vs. concentration in the GB, c_{GB} at 300 K using CSP for GB atom selection.
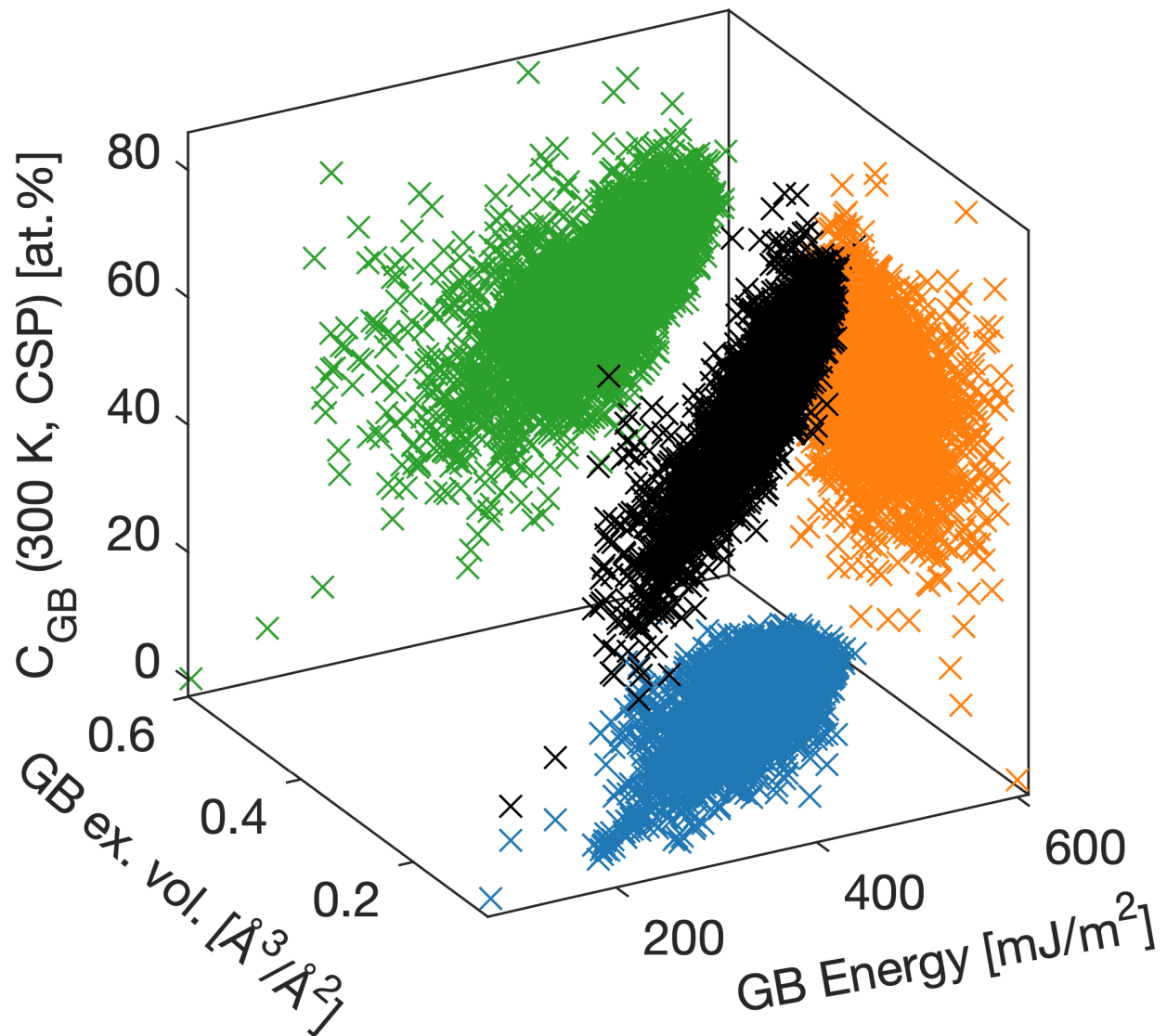
Figure 4.6 Concentration of solute at the GB, c_{GB}, as a function of GB excess volume and GB energy. The following are projected onto their corresponding planes: c_{GB} vs. GB energy (green), c_{GB} vs. GB excess volume (orange), and GB excess volume vs. GB energy (blue).

Chapter 5

Conclusions

In this work, we examined grain boundary segregation energy spectra of Co in 7272 Al GBs that comprehensively sample the 5D space of crystallographic character. This included calculating segregation energies for more than 70 million possible sites.

Verification of the dataset involved determining how to identify bulk vs. GB atoms. While aCNA is often used for bulk determination in GBs, the number of non-negligible segregation energies that were excluded by aCNA categorization caused us to consider CSP as an alternative, with a cutoff of 0.1 for bulk determination. The differences between these two methods are illustrated in Figures 3.1 and 3.2 and discussed further in Supplemental Section S1. The resulting segregation energy spectra from both methods were also compared in Figures 3.4, 3.5 and 4.3b. It was determined that they give similar answers despite the reduced number of atoms included by aCNA, as illustrated in a comparison of c_{GB} values calculated by both CSP and aCNA shown in Supplemental Figure S16. However, the small differences point to a need for the community to address GB atom selection when examining segregation energy spectra and consider possible alternatives such as a fixed width approach, which best matches the low disorientation angle c_{GB} expectations (c.f. Supplemental Figure S18). Such efforts by the community may help determine the optimal approach to extracting segregation energy distributions from both bicrystal and polcrystalline simulations. Verification

also involved removing invalid segregation energy calculations that did not converge to 0 eV at large distances from the GB, since they do not match the expected behavior [62, 63], and GBs with unreasonably low segregation energies. The complete list of GBs excluded from analysis in this work is given in Supplemental Table S3.

Validation involved comparing the computed GB segregation energies to similar bicrystal and polycrystal computational studies. In Figure 3.4 it was shown that a subset of the data produced in this work is similar to the work of Huber et al. in [31]. The aggregated spectrum of segregation energies in the Homer bicrystal GB dataset is also similar to the segregation energy spectrum in polycrystals obtained by Wagih et al. in [27], as shown in Figure 3.5 and Table 3.1. Both validation comparisons are favorable, but some minor differences between the polycrystal and bicrystal spectra raise a number of questions, posed in Section 3.2, that are worth resolving and that could impact the quality of an aggregate segregation energy spectrum.

Several insights arose from different methods of analysis. Figure 4.1 shows that as GB energy increases, Co segregation in Al GBs becomes more favorable. This is supported by the increase of c_{GB} with GB energy shown in Figure 4.2b, Figure 4.6, and Supplemental Figure S17. Additionally, all of the GBs have higher c_{GB} than c_{bulk}, except the [111] symmetric twist perfect twin GB. Figure 4.2b shows that most GBs have a preference for segregation, evidenced by their proximity to the "all segregating" corner of the plot. However, there are some some interesting GBs that are outliers, many of which have [100], [110], and [111] disorientation axes. The most extreme outlier is the [111] twin GB that is located at "all anti-segregating". In addition, the temperature dependence of c_{GB} was demonstrated in Figure 4.3c, which shows that c_{GB} drops dramatically at higher temperatures.

In general, it was found that c_{GB} has smooth variation across the 5D space of crystallographic character (see Figure 4.4 and Supplemental Figure S19). Additional examination confirmed that c_{GB} can be described in a linear model with GB energy and GB excess volume (see Figure 4.6 and Table

4.4), which linear model finds no correlation with disorientation angle (see Supplemental Figure S18) across the 5D space. c_{GB} does not have an obvious functional form in 5D crystallographic space, which is shown by the rugged landscapes in Figure 4.4 and the lack of obvious trends in Supplemental Figure S19. This emergence of local but not global trends may or may not be inline with the limited experimental datasets available in the literature, as discussed above; additional data will be required to verify such conclusions.

Appendix A

Comparison of bulk atom selection by aCNA and CSP

To contrast the differences between bulk atom selection by aCNA and CSP, we examine a few different items. First, we note that 90% of the atoms classified as bulk FCC by aCNA have CSP values less than 0.1, as illustrated in Supplemental Figure A.1. However, the remaining 10% of atoms classified as bulk FCC by aCNA can have CSP values as high as 5, indicating the tendency for aCNA to tolerate some noise in the classification of environments as as the FCC structure. Second, we present a contingency table in Figure A.2 showing that of the 70 million atoms simulated, only 17% (11.5 million) were classified by aCNA as GB atoms, compared to the 26% (18 million) atoms classified as GB atoms by CSP. This also results in a larger bulk atom population for aCNA than CSP. The segregation energy spectrum for these bulk atoms by both classification schemes is illustrated in Figure 3.2. The aCNA spectrum is slightly wider than the CSP spectrum because atoms with larger structural distortions and therefore a wider distribution of segregation energies are categorized as FCC by the aCNA classifier. In short, the aCNA and CSP give fairly similar results, with aCNA being more restrictive in its selection of GB atoms and therefore leaving out

some atoms with non-negligble segregation energies. On the other hand, classification of bulk atoms by CSP ≤ 0.1 results in a more generous selection of GB atoms that capture the segregation energy deviations left out by aCNA. But, this comes at the cost of having more GB atoms with very small segregation energies. The effect of these near-negligible segregation energies on the c_{GB} in the CSP spectra is shown in Supplemental Figure B.9; CSP predicts lower c_{GB} values, however any trends in c_{GB} appear to be the same whether CSP or aCNA were used due to the positive correlation between the two methods. Perhaps a more restrictive CSP value might bridge this difference better but we do not attempt to fine tune the CSP value in this work.
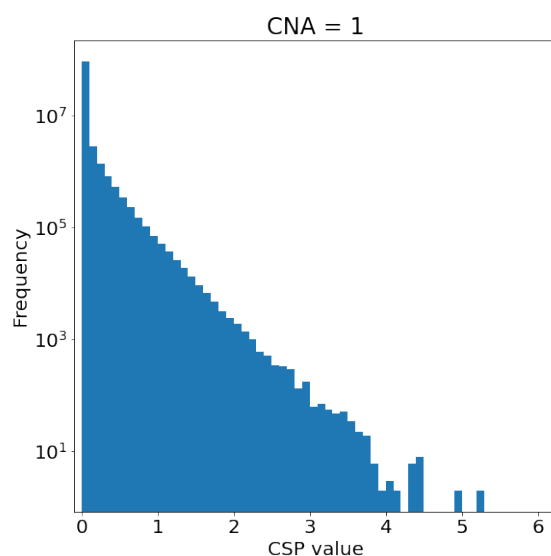
Figure A.1 Logarithmic scale of the distribution of centrosymmetry parameters (CSP) for FCC atoms as determined by aCNA. The bin size is 0.1. Only 7% of FCC atoms determined by aCNA have a CSP greater than 0.1.

CSP

		GB	Bulk	
aCNA	GB	11.5M	0	11.5M 17%
	Bulk	6.5M	51M	57.5M 83%
		18M 26%	51M 74%	

Figure A.2 Contingency table comparing CSP and aCNA bulk atom determination. All atoms determined by aCNA to be bulk are also classified as bulk by CSP, although aCNA includes 6.5 million additional atoms in the bulk category.
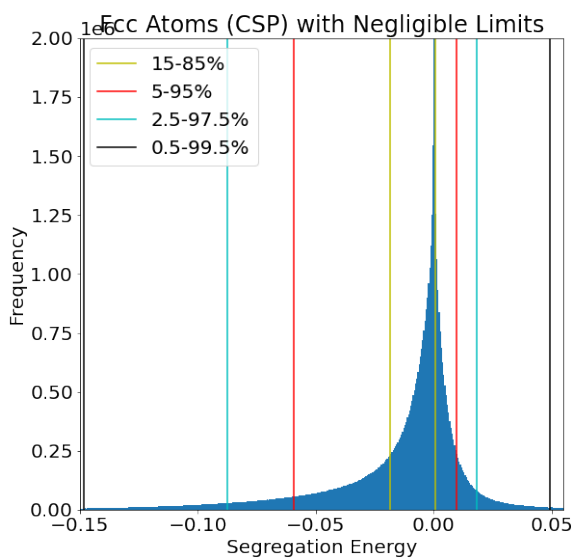
Figure A.3 Distribution of segregation energies for FCC atoms as determined by CSP. Different intervals are shown. This work uses the 95% interval for the limits of the "negligible segregation" category (-0.040 eV $\leq E_{\text{seg}}^{\text{Co}_i} < +0.0115$ eV).
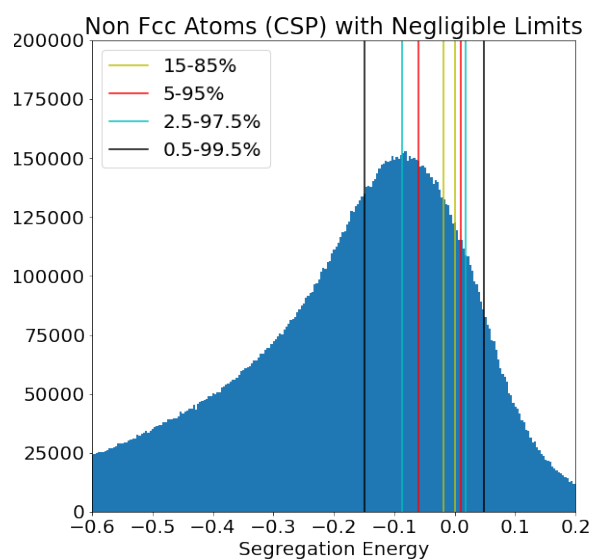
Figure A.4 Distribution of segregation energies for non-FCC atoms as determined by CSP. Different intervals of the distribution of segregation energies for FCC atoms as determined by CSP are shown. This work uses the 95% interval for the limits of the "negligible segregation" category (-0.040 eV $\leq E_{\text{seg}}^{\text{Co}_i} < +0.0115$ eV).

Appendix B

Supplemental Figures
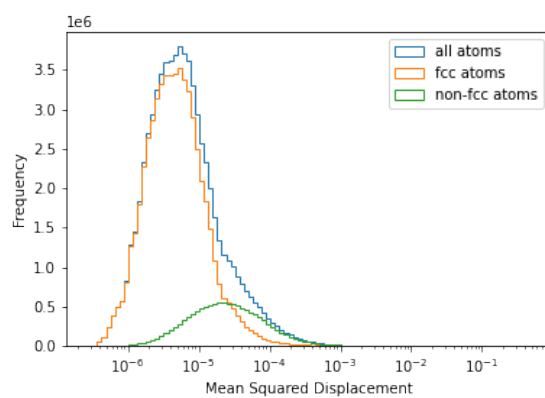
Figure B.1 Mean Squared Displacement distribution of all atoms (blue) all FCC atoms as determined by aCNA (orange), and all non-FCC GB atoms (green). All of the distributions are approximately log normal.
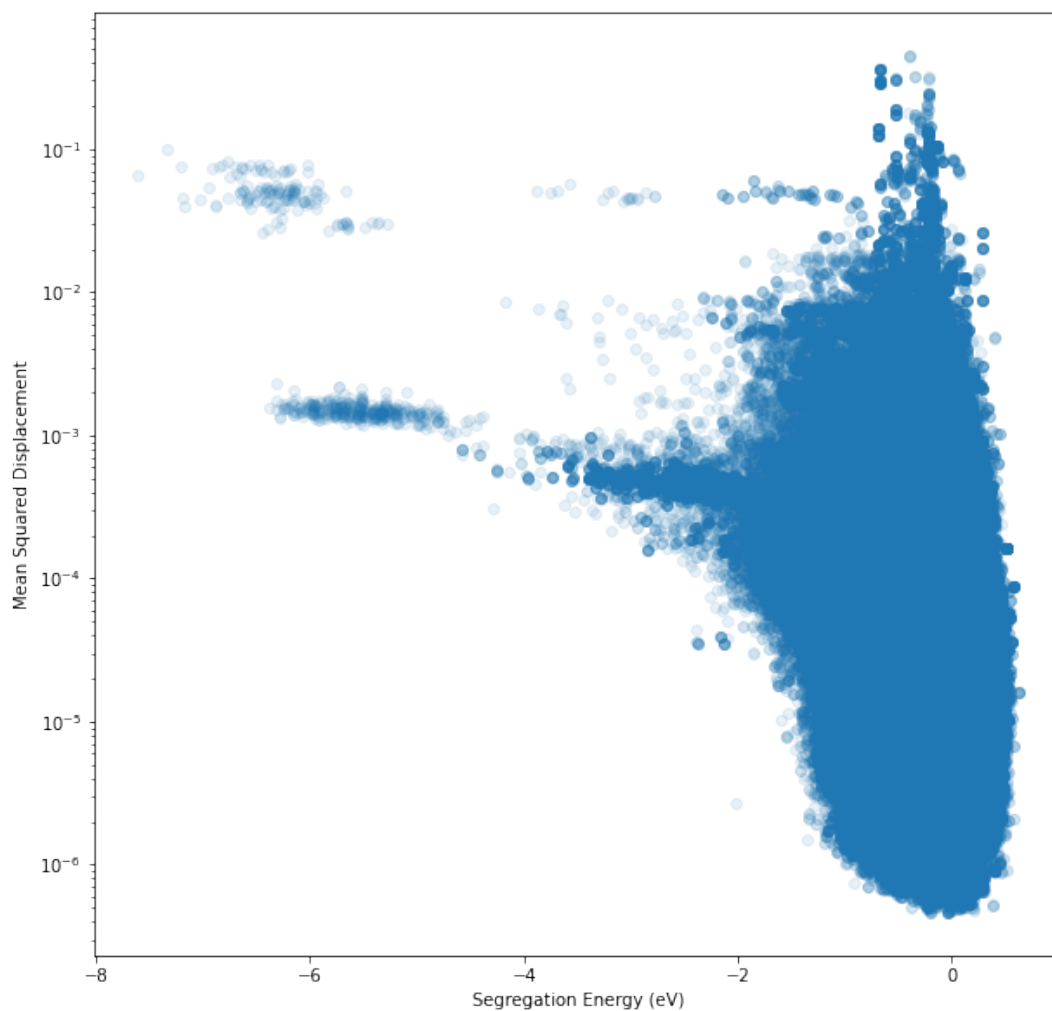
Figure B.2 Scatter plot of mean squared displacement (MSD) vs. segregation energy ($E_{\text{seg}}^{\text{Co}_i}$) for all non-FCC atoms. This scatter plot was used to decide on a (later discarded) "high-MSD" cutoff for atoms to remove from analysis, noting that the approximately skew-normal distribution of segregation energies was interrupted mostly by atoms with MSD $> 10^{-4}$, which was decided somewhat arbitrarily to be the "high-MSD" cutoff value considered in this work.
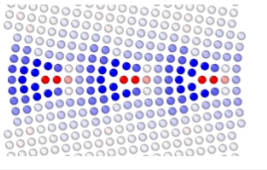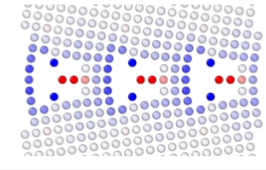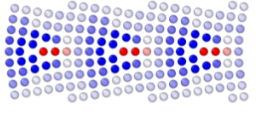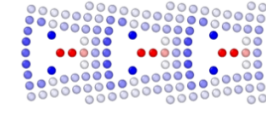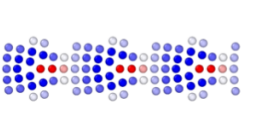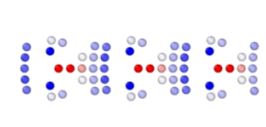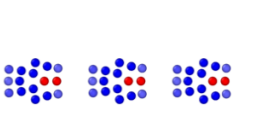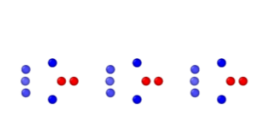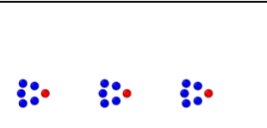
	All atoms	No high-msd atoms
All atoms		
CSP >= 0.01		
CSP >= 0.1		
CSP >= 0.3		
CNA		

Figure B.3 A [100] symmetric tilt GB with an array of edge dislocations with all atoms, and bulk atoms cut out using 4 different techniques: CSP ≤ 0.3, CSP ≤ 0.1, CSP ≤ 0.01, and aCNA. The right side also cuts out atoms according to the high-MSD cutoff of 10^{-4}. Red atoms have positive segregation energies, blue have negative, and grey have negligible, according to the colorbar shown. On the right, using the combination of high-MSD and CNA, only one atom per structural unit [88–94] in the GB remains to analyze, giving the impression that the entire GB is unfavorable to solute segregation (red coloring corresponds to anti-segregation), when other removal methods show that the GB contains many other sites favorable to solute segregation (blue colored atom sites). Such aggressive atom removal via aCNA and MSD caused the authors to consider other methods of atom removal, discussed in Sections 3.1 and 3.1.
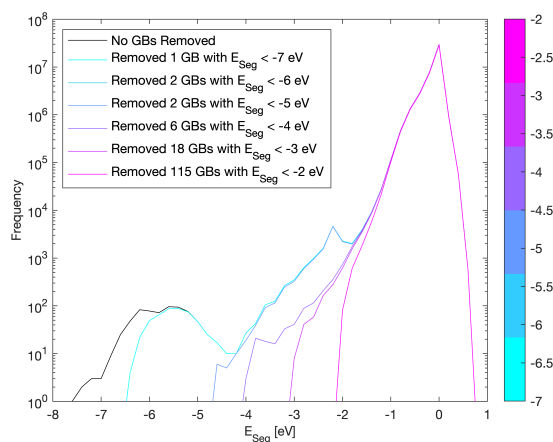
Figure B.4 Spectrum of segregation energies for the entire Homer GB dataset [52], with all atoms from GBs below several different cutoffs removed. A high concentration of extreme segregation energy values were found in several GBs. The authors chose to remove 18 GBs.
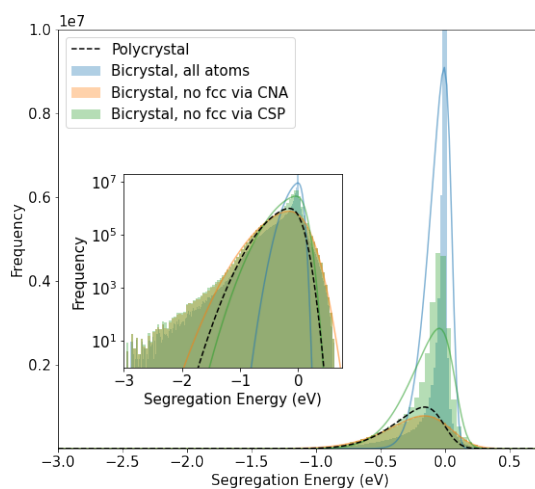
Figure B.5 The spectrum of segregation energies aggregated from all GBs simulated in this work, including bulk atoms (blue), with all bulk atoms removed via aCNA (orange), and via CSP (green). The dotted line is the polycrystal spectrum from Wagih et al. in [27]. Compare to Figure 3.5

.
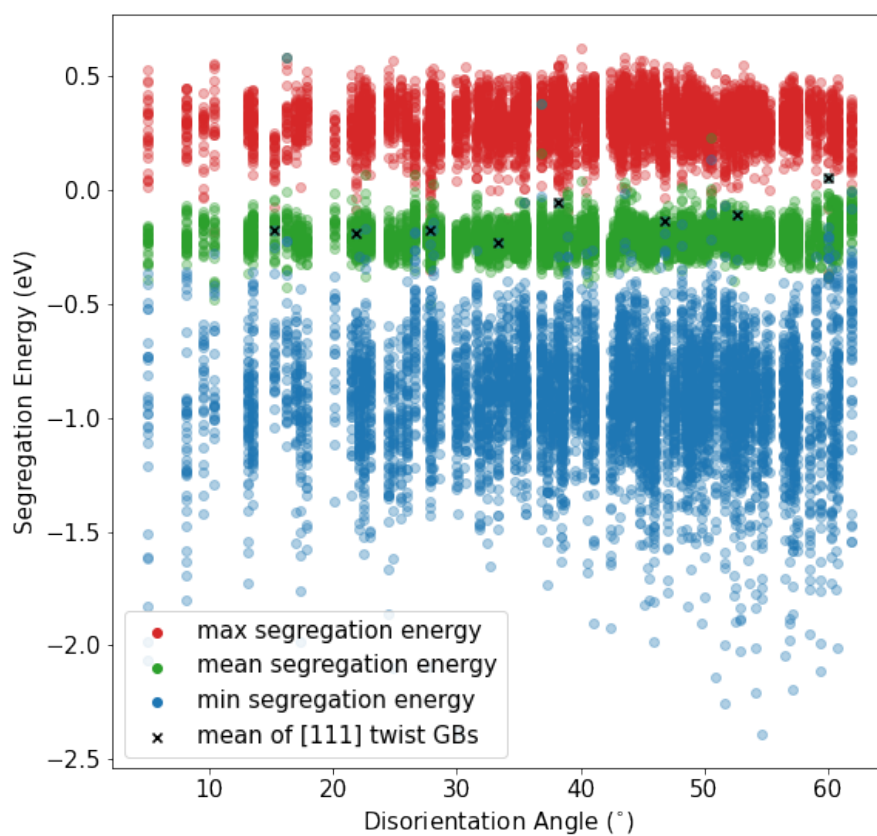
Figure B.6 Minimum (blue), maximum (red), and mean (green) of segregation energy $E_{\text{seg}}^{\text{Co}_i}$ vs. their disorientation angle. [111] symmetric twist GBs marked by black "x"s.
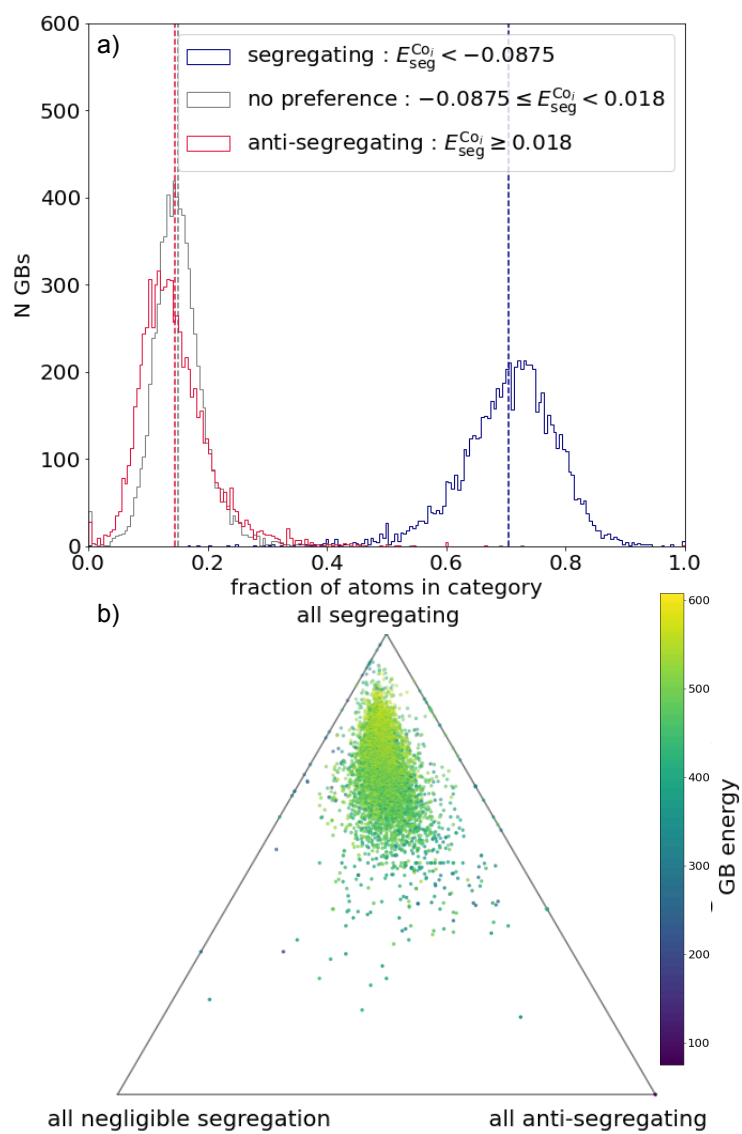
Figure B.7 Ternary Plot for CNA.
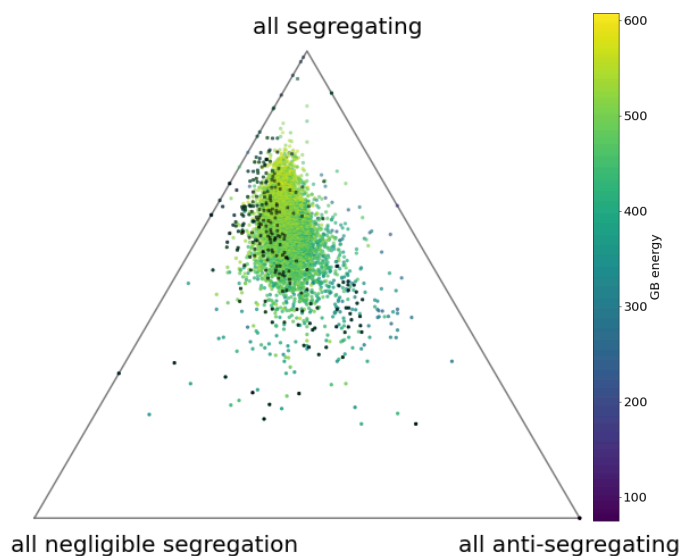
Figure B.8 Ternary Plot for CSP with the [111] disorientation axis GBs shown in black.
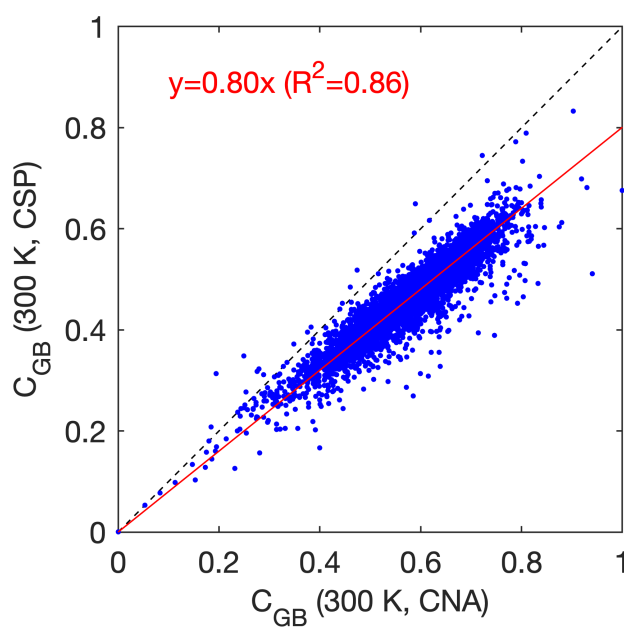
Figure B.9 Correlation plot between c_{GB} as calculated using GB atoms determined by aCNA (x-axis) and CSP (y-axis) for all 7272 GBs. CSP bulk determination includes more negligibly segregating atom sites, and therefore has a lower c_{GB} than the corresponding value for aCNA bulk determination, with a correlation of $c_{GB}^{CSP} = .8 c_{GB}^{aCNA}$.
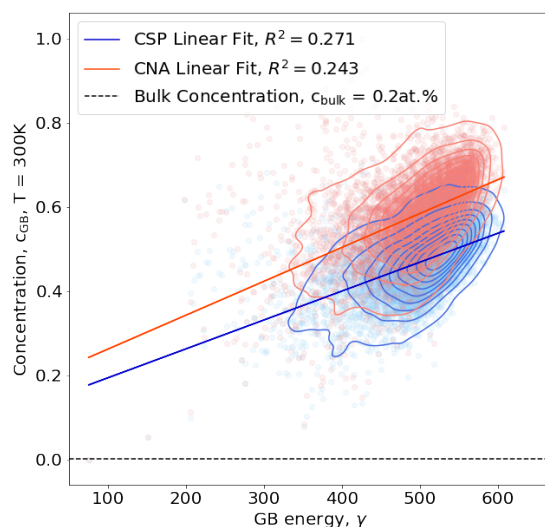
Figure B.10 Concentration of solute at the GB, c_{GB} (shown in fractions, not at%), vs. GB energy, γ, for all GBs in the Homer dataset [52] at T = 300 K, for aCNA (red) and CSP (blue) bulk atom determination. Density contours overlaid, with linear fit line with R^2 values indicated in the legend. All GBs except the [111] symmetric twist perfect twin have a higher concentration, c_{GB}, than c_{bulk}=0.2at%, shown with a black dotted line.
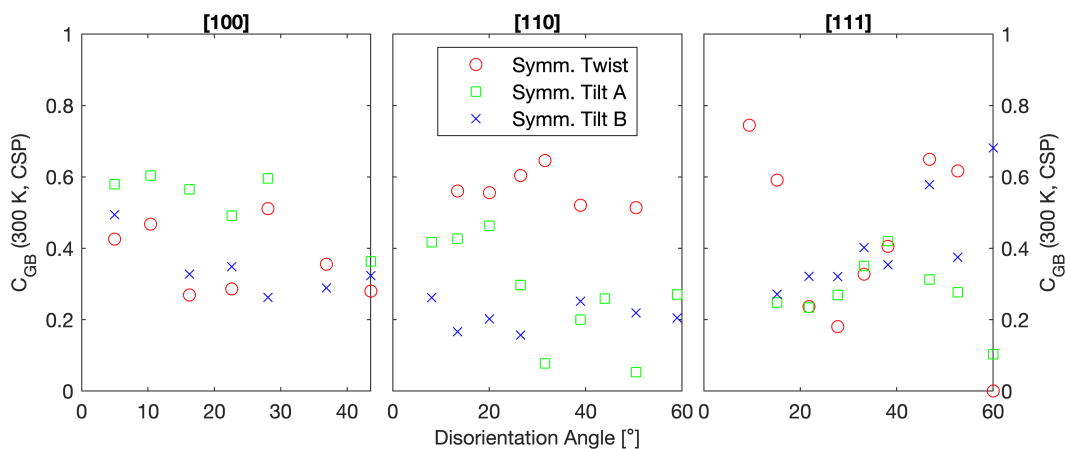

Figure B.11 c_{GB} (CSP) vs. disorientation angle (°) for 9 special types of GBs: the symmetric twist GBs (red) and the symmetric tilt GBs (green + blue) for the [100], [110], and [111] disorientation axes. None of these subsets demonstrate the general trends very well, but the [111] symmetric twist GBs are noted in the main body of this paper for illustration purposes. (Note: given are the disorientation angles about the disorientation axes but for the symmetric tilt GBs, their tilt angle is a derived quantity.)
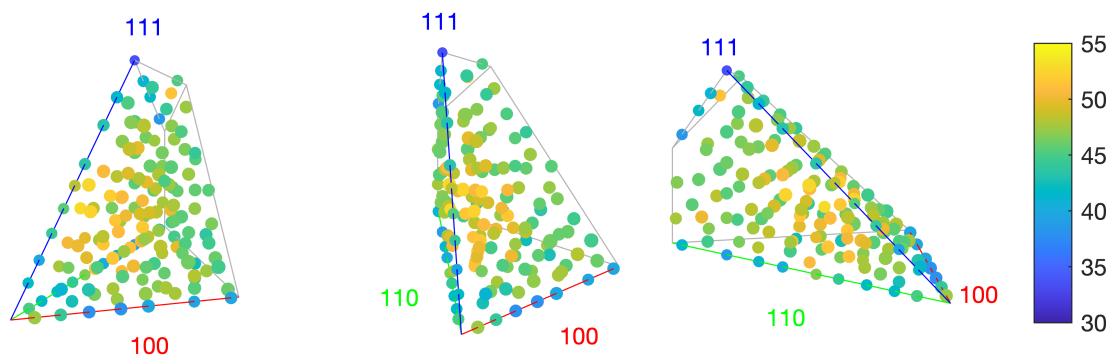
Figure B.12 Multiple views of c_{GB} (100×at%) in Rodriguez-Frank space. The following disorientation axes are found along the corresponding (color)ed lines: [100] (red), [110] (green), [111] (blue).

Figure B.13 Concentration of solute at the GB, c_{GB}, as a function of disorientation angle.

Table B.1 GBs excluded from the Al Homer dataset [52]. The CSL value, disorientation (dis.) angle and axis, and boundary plane normals from both sides of the grain N_A / N_B are provided, along with the reason the GB is excluded from the analysis.

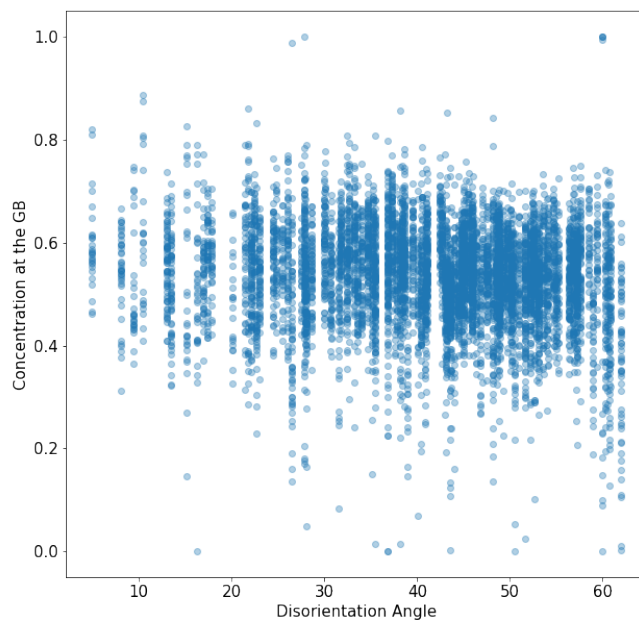| CSL	Dis. angle and axis	N_A / N_B	Reason excluded
$\Sigma 145h$	$56.5°\,[6\,5\,2]$	$(29\,165\,153)\,/\,(\overline{5}\,\overline{45}\,\overline{3})$	Refill Issues
$\Sigma 265a$	$5.0°\,[1\,0\,0]$	$(0\,\overline{37}\,56)\,/\,(0\,32\,\overline{59})$	Refill Issues
$\Sigma 265a$	$5.0°\,[1\,0\,0]$	$(265\,\overline{293}\,379)\,/\,(\overline{265}\,259\,\overline{403})$	Refill Issues
$\Sigma 265a$	$5.0°\,[1\,0\,0]$	$(265\,\overline{239}\,727)\,/\,(\overline{5}\,35\,\overline{149})$	Refill Issues
$\Sigma 265a$	$5.0°\,[1\,0\,0]$	$(265\,\overline{215}\,1235)\,/\,(\overline{265}\,107\,\overline{1249})$	Refill Issues
$\Sigma 303a$	$24.8°\,[3\,2\,1]$	$(\overline{58}\,85\,307)\,/\,(106\,\overline{191}\,\overline{239})$	Refill Issues
$\Sigma 441o$	$49.2°\,[11\,4\,4]$	$(269\,\overline{212}\,\overline{638})\,/\,(\overline{269}\,638\,212)$	Refill Issues
$\Sigma 647q$	$60.3°\,[9\,9\,1]$	$(141\,\overline{185}\,396)\,/\,(185\,\overline{141}\,\overline{396})$	Refill Issues
$\Sigma 943l$	$38.4°\,[10\,1\,1]$	$(117\,76\,\overline{303})\,/\,(\overline{135}\,132\,275)$	Refill Issues
$\Sigma 999ae$	$58.5°\,[16\,11\,10]$	$(721\,\overline{61}\,587)\,/\,(\overline{685}\,625\,\overline{91})$	Refill Issues
$\Sigma 131e$	$60.3°\,[5\,5\,4]$	$(21\,\overline{1147}\,1211)\,/\,(1157\,\overline{39}\,\overline{1201})$	Conv. Issues
$\Sigma 131e$	$60.3°\,[5\,5\,4]$	$(\overline{97}\,\overline{703}\,869)\,/\,(833\,\overline{137}\,\overline{739})$	Conv. Issues
$\Sigma 265a$	$5.0°\,[1\,0\,0]$	$(265\,\overline{63}\,389)\,/\,(\overline{265}\,29\,\overline{393})$	Conv. Issues
$\Sigma 549h$	$32.4°\,[13\,1\,1]$	$(139\,\overline{5}\,\overline{155})\,/\,(\overline{143}\,91\,121)$	Conv. Issues
$\Sigma 55b$	$38.6°\,[2\,1\,1]$	$(\overline{39}\,38\,\overline{70})\,/\,(110\,88)$	Low E_{seg} Values
$\Sigma 55c$	$57.6°\,[5\,5\,1]$	$(67\,\overline{26}\,70)\,/\,(\overline{4}\,\overline{32}\,\overline{95})$	Low E_{seg} Values
$\Sigma 55c$	$57.6°\,[5\,5\,1]$	$(109\,\overline{117}\,95)\,/\,(9\,17\,\overline{185})$	Low E_{seg} Values
$\Sigma 73b$	$13.4°\,[1\,1\,0]$	$(192\,\overline{119}\,114)\,/\,(\overline{169}\,96\,\overline{162})$	Low E_{seg} Values
$\Sigma 73b$	$13.4°\,[1\,1\,0]$	$(235\,\overline{89}\,119)\,/\,(\overline{211}\,65\,\overline{169})$	Low E_{seg} Values
$\Sigma 73e$	$48.9°\,[4\,3\,0]$	$(\overline{507}\,311\,331)\,/\,(543\,\overline{359}\,199)$	Low E_{seg} Values
$\Sigma 83d$	$57.2°\,[3\,3\,1]$	$(259\,\overline{681}\,685)\,/\,(429\,65\,\overline{901})$	Low E_{seg} Values

CSL	Dis. angle and axis	N_A / N_B	Reason excluded
$\Sigma 145h$	$56.5°\,[6\,5\,2]$	$\left(609\,\overline{515}\,\overline{467}\right) / \left(\overline{477}\,695\,\overline{379}\right)$	Low E_{seg} Values
$\Sigma 145h$	$56.5°\,[6\,5\,2]$	$\left(29\,\overline{55}\,123\right) / \left(53\,\overline{45}\,\overline{119}\right)$	Low E_{seg} Values
$\Sigma 197g$	$54.1°\,[9\,9\,1]$	$\left(291\,\overline{11}\,41\right) / \left(\overline{205}\,57\,\overline{203}\right)$	Low E_{seg} Values
$\Sigma 197g$	$54.1°\,[9\,9\,1]$	$\left(248\,\overline{335}\,586\right) / \left(215\,\overline{118}\,\overline{676}\right)$	Low E_{seg} Values
$\Sigma 197g$	$54.1°\,[9\,9\,1]$	$\left(111\,\overline{451}\,499\right) / \left(307\,45\,\overline{607}\right)$	Low E_{seg} Values
$\Sigma 201a$	$8.1°\,[1\,1\,0]$	$\left(241\,\overline{40}\,197\right) / \left(\overline{220}\,19\,\overline{223}\right)$	Low E_{seg} Values
$\Sigma 201a$	$8.1°\,[1\,1\,0]$	$\left(779\,\overline{377}\,103\right) / \left(\overline{763}\,361\,\overline{217}\right)$	Low E_{seg} Values
$\Sigma 215e$	$45.9°\,[9\,7\,1]$	$\left(\overline{189}\,323\,\overline{345}\right) / \left(\overline{9}\,\overline{9}\,101\right)$	Low E_{seg} Values
$\Sigma 265a$	$5.0°\,[1\,0\,0]$	$\left(265\,\overline{689}\,1007\right) / \left(\overline{265}\,599\,\overline{1063}\right)$	Low E_{seg} Values
$\Sigma 283f$	$44.7°\,[9\,1\,0]$	$\left(\overline{515}\,107\,273\right) / \left(531\,\overline{251}\,\overline{79}\right)$	Low E_{seg} Values
$\Sigma 303a$	$24.8°\,[3\,2\,1]$	$\left(\overline{46}\,151\,139\right) / \left(50\,\overline{193}\,\overline{67}\right)$	Low E_{seg} Values

Data Availability

The datasets for the current study are available in the Mendeley Data repository. The GB structures analyzed in the study are available at https://doi.org/10.17632/4ykjz4ngw [52, 57] and the dataset containing all of the per GB quantities computed in this work, including the c_{GB} values and a histogram of each GB's segregation spectrum, is available at https://doi.org/10.17632/rf3bt5f4hd [95].

Bibliography

[1] F. J. Humphreys and M. Hatherly, *Recrystallization and Related Annealing Phenomena*, 2nd ed. (Elsevier, Boston, 2004).

[2] K. Lücke and K. Detert, "A quantitative theory of grain-boundary motion and recrystallization in metals in the presence of impurities," Acta Metallurgica **5,** 628–637 (1957).

[3] F. Liu and R. Kirchheim, "Nano-scale grain growth inhibited by reducing grain boundary energy through solute segregation," Journal of Crystal Growth **264,** 385–391 (2004).

[4] A. R. Kalidindi and C. A. Schuh, "Stability criteria for nanocrystalline alloys," Acta Materialia **132,** 128–137 (2017).

[5] J. Weissmüller, "Alloy thermodynamics in nanostructures," Journal of Materials Research **9,** 4–7 (1994).

[6] J. Weissmüller, "Some basic notions on nanostructured solids," Materials Science and Engineering: A **179,** 102–107 (1994).

[7] S. Ruan and C. A. Schuh, "Electrodeposited Al-Mn alloys with microcrystalline, nanocrystalline, amorphous and nano-quasicrystalline structures," Acta Materialia **57,** 3810–3822 (2009).

[8] T. Chookajorn, H. A. Murdoch, and C. A. Schuh, "Design of Stable Nanocrystalline Alloys," Science **337,** 951–954 (2012).

[9] Y. Shi, H. Xue, F. Tang, X. Lu, J. Ren, and J. Li, "Effects of transition metal segregation on the thermodynamic stability and strength of Ni Σ11 [110](113) symmetrical tilt grain boundary," Vacuum **212,** 112036 (2023).

[10] E. O. Hall, "The Deformation and Ageing of Mild Steel: III Discussion of Results," Proceedings of the Physical Society. Section B **64,** 747–753 (1951).

[11] N. J. Petch, "The Cleavage Strength of Polycrystals," Journal of the Iron and Steel Institute **174,** 25–28 (1953).

[12] A. E. Perrin and C. A. Schuh, "Stabilized nanocrystalline alloys: The intersection of grain boundary segregation with processing science," Annual Review of Materials Research **51,** 241–268 (2021).

[13] D. McLean, *Grain Boundary Segregation in Metals* (Clarendon Press, Oxford, 1957).

[14] J. Friedel, "Electronic structure of primary solid solutions in metals," Advances in Physics **3,** 446–507 (1954).

[15] M. Seah, "Adsorption-induced interface decohesion," Acta Metallurgica **28,** 955–962 (1980).

[16] H. Erhart and H.-J. Grabke, "Equilibrium segregation of phosphorus at grain boundaries of Fe–P, Fe–C–P, Fe–Cr–P, and Fe–Cr–C–P alloys," Metal science **15,** 401–408 (1981).

[17] T. Muschik, S. Hofmann, W. Gust, and B. Predel, "Surface and grain boundary segregation in Ni–In studied under identical conditions with AES," Applied Surface Science **37,** 439–455 (1989).

[18] F. Christien, R. Le Gall, and G. Saindrenan, "Phosphorus grain boundary segregation in steel 17-4PH," Scripta Materialia **48,** 11–16 (2003).

[19] J. D. Robson, "Effect of rare-earth additions on the texture of wrought magnesium alloys: the role of grain boundary segregation," Metallurgical and Materials Transactions A **45,** 3205–3212 (2014).

[20] P. Lejček, *Grain Boundary Segregation in Metals* (Springer-Verlag, Berlin, 2010).

[21] M. Wagih and C. A. Schuh, "Thermodynamics and design of nanocrystalline alloys using grain boundary segregation spectra," Acta Materialia **217,** 117177 (2021).

[22] C. White and W. Coghlan, "Spectrum of binding energies approach to grain boundary segregation," Metallurgical Transactions A **8,** 1403–1412 (1977).

[23] T. Mütschele and R. Kirchheim, "Segregation and diffusion of hydrogen in grain boundaries of palladium," Scripta Metallurgica **21,** 135–140 (1987).

[24] R. Kirchheim, "Hydrogen solubility and diffusivity in defective and amorphous metals," Progress in Materials Science **32,** 261–325 (1988).

[25] M. S. Titus, R. K. Rhein, P. B. Wells, P. C. Dodge, G. B. Viswanathan, M. J. Mills, A. Van der Ven, and T. M. Pollock, "Solute segregation and deviation from bulk thermodynamics at nanoscale crystalline defects," Science Advances **2,** 1601796 (2016).

[26] M. Wagih and C. A. Schuh, "Spectrum of grain boundary segregation energies in a polycrystal," Acta Materialia **181,** 228–237 (2019).

[27] M. Wagih, P. M. Larsen, and C. A. Schuh, "Learning grain boundary segregation energy spectra in polycrystals," Nature Communications **11,** 6376 (2020).

[28] M. Wagih and C. A. Schuh, "The spectrum of interstitial solute energies in polycrystals," Scripta Materialia **235,** 115631 (2023).

[29] K. Ito, Y. Tanaka, K. Tsutsui, and H. Sawada, "Analysis of grain-boundary segregation of hydrogen in bcc-Fe polycrystals via a nano-polycrystalline grain-boundary model," Computational Materials Science **225,** 112196 (2023).

[30] N. Tuchinda and C. A. Schuh, "Computed entropy spectra for grain boundary segregation in polycrystals," npj Computational Materials **10,** 72 (2024).

[31] L. Huber, R. Hadian, B. Grabowski, and J. Neugebauer, "A machine learning approach to model solute grain boundary segregation," npj Computational Materials **4,** 64 (2018).

[32] Y. Mahmood, M. Alghalayini, E. Martinez, C. J. Paredis, and F. Abdeljawad, "Atomistic and machine learning studies of solute segregation in metastable grain boundaries," Scientific Reports **12,** 6673 (2022).

[33] Y. Cui, K. Song, Y. Bao, Y. Zhu, Q. Liu, and P. Qian, "Effect of Cu and Mg co-segregation on the strength of the Al grain boundaries: A molecular dynamics simulation," Computational Materials Science **229,** 112391 (2023).

[34] J. Zhang, Y. Jiang, Z. Liu, and Y. Wang, "Weight-averaged solute segregations at grain boundaries in advanced ferritic alloys," Surfaces and Interfaces **41,** 103235 (2023).

[35] V. Menon, S. Das, V. Gavini, and L. Qi, "Atomistic simulations and machine learning of solute grain boundary segregation in Mg alloys at finite temperatures," Acta Materialia **264,** 119515 (2024).

[36] L. Karkina, I. Karkin, A. Kuznetsov, I. Razumov, P. A. Korzhavyi, and Y. N. Gornostyrev, "Solute–grain boundary interaction and segregation formation in Al: First principles calcu-

lations and molecular dynamics modeling," Computational Materials Science **112,** 18–26 (2016).

[37] R. Mahjoub, K. J. Laws, N. Stanford, and M. Ferry, "General trends between solute segregation tendency and grain boundary character in aluminum-An ab inito study," Acta Materialia **158,** 257–268 (2018).

[38] J. Zhang, Y. Dou, and Y. Zheng, "Twin-boundary segregation energies and solute-diffusion activation enthalpies in Mg-based binary systems: a first-principles study," Scripta Materialia **80,** 17–20 (2014).

[39] L. Huber, B. Grabowski, M. Militzer, J. Neugebauer, and J. Rottler, "Ab initio modelling of solute segregation energies to a general grain boundary," Acta Materialia **132,** 138–148 (2017).

[40] Z. Xiao, L. He, and X.-M. Bai, "First principle studies of effects of solute segregation on grain boundary strength in Ni-based alloys," Journal of Alloys and Compounds **874,** 159795 (2021).

[41] V. Fotopoulos, J. Strand, M. Petersmann, and A. L. Shluger, "First principles study on the segregation of metallic solutes and non-metallic impurities in Cu grain boundary," In *TMS Annual Meeting & Exhibition*, pp. 989–999 (2024).

[42] R. Pei, Z. Xie, S. Yi, S. Korte-Kerzel, J. Guénolé, and T. Al-Samman, "Atomistic insights into the inhomogeneous nature of solute segregation to grain boundaries in magnesium," Scripta Materialia **230,** 115432 (2023).

[43] C. M. Barr, S. M. Foiles, M. Alkayyali, Y. Mahmood, P. M. Price, D. P. Adams, B. L. Boyce, F. Abdeljawad, and K. Hattar, "The role of grain boundary character in solute segregation and thermal stability of nanocrystalline Pt–Au," Nanoscale **13,** 3552–3563 (2021).

[44] M. Wagih, Y. Naunheim, T. Lei, and C. A. Schuh, "Grain boundary segregation predicted by quantum-accurate segregation spectra but not by classical models," Acta Materialia **266,** 119674 (2024).

[45] Z. Zhang and C. Deng, "Grain boundary segregation prediction with a dual-solute model," arXiv preprint arXiv:2404.15513 (2024).

[46] W. Xing, A. R. Kalidindi, D. Amram, and C. A. Schuh, "Solute interaction effects on grain boundary segregation in ternary alloys," Acta Materialia **161,** 285–294 (2018).

[47] P. Lejček, M. Šob, and V. Paidar, "Interfacial segregation and grain boundary embrittlement: An overview and critical assessment of experimental data and calculated results," Progress in Materials Science **87,** 83–139 (2017).

[48] C. Hu, R. Dingreville, and B. L. Boyce, "Computational modeling of grain boundary segregation: A review," Computational Materials Science **232,** 112596 (2024).

[49] M. Wagih and C. A. Schuh, "Learning grain-boundary segregation: From first principles to polycrystals," Physical Review Letters **129,** 046102 (2022).

[50] J. Tavenner, A. Gupta, and G. Tucker, TMS Annual Meeting & Exhibition, Anaheim California (unpublished).

[51] M. Wagih and C. A. Schuh, "Can symmetric tilt grain boundaries represent polycrystals?," Scripta Materialia **237,** 115716 (2023).

[52] E. R. Homer, G. L. W. Hart, D. Hensley, C. B. Owens, and L. H. Serafin, "Computed Al Grain Boundary Structures and Energies Covering 5D Space,", Mendeley Data, 2022, v1.

[53] T. Watanabe and S. Tsurekawa, "The control of brittleness and development of desirable mechanical properties in polycrystalline systems by grain boundary engineering," Acta materialia **47,** 4171–4185 (1999).

[54] A. K. Sfikas, S. Gonzalez, A. G. Lekatou, S. Kamnis, and A. E. Karantzalis, "A Critical Review on Al-Co Alloys: Fabrication Routes, Microstructural Evolution and Properties," Metals **12,** 1092 (2022).

[55] K. Geng, Y. Yang, S. Li, R. Misra, and Q. Zhu, "Enabling high-performance 3D printing of Al powder by decorating with high laser absorbing Co phase," Additive Manufacturing **32,** 101012 (2020).

[56] P. Lejček and S. Hofmann, "Thermodynamics and structural aspects of grain boundary segregation," Critical Reviews in Solid State and Material Sciences **20,** 1–85 (1995).

[57] E. R. Homer, G. L. Hart, C. Braxton Owens, D. M. Hensley, J. C. Spendlove, and L. H. Serafin, "Examination of computed aluminum grain boundary structures and energies that span the 5D space of crystallographic character," Acta Materialia **234,** 118006 (2022).

[58] Y. Mishin, D. Farkas, M. J. Mehl, and D. A. Papaconstantopoulos, "Interatomic potentials for monoatomic metals from experimental data and ab initio calculations," Physical Review B **59,** 3393–3407 (1999).

[59] A. P. Thompson *et al.*, "LAMMPS - a flexible simulation tool for particle-based materials modeling at the atomic, meso, and continuum scales," Comp. Phys. Comm. **271,** 108171 (2022).

[60] G. Purja Pun, V. Yamakov, and Y. Mishin, "Interatomic potential for the ternary Ni–Al–Co system and application to atomistic modeling of the B2–L10 martensitic transformation," Modelling and Simulation in Materials Science and Engineering **23,** 065006 (2015).

[61] A. Tamm, A. Aabloo, M. Klintenberg, M. Stocks, and A. Caro, "Atomic-scale properties of Ni-based FCC ternary, and quaternary alloys," Acta Materialia **99,** 307–312 (2015).

[62] H. Jin, I. Elfimov, and M. Militzer, "Study of the interaction of solutes with Σ5 (013) tilt grain boundaries in iron using density-functional theory," Journal of Applied Physics **115,** 093506 (2014).

[63] D. Scheiber, V. I. Razumovskiy, P. Puschnig, R. Pippan, and L. Romaner, "Ab initio description of segregation and cohesion of grain boundaries in W–25 at.% Re alloys," Acta Materialia **88,** 180–189 (2015).

[64] M. Seah and E. Hondros, "Grain boundary segregation," Proceedings of the Royal Society of London. A. Mathematical and Physical Sciences **335,** 191–212 (1973).

[65] D. Scheiber, M. N. Popov, and L. Romaner, "Temperature dependence of solute segregation energies at W GBs from first principles," Scripta materialia **222,** 115059 (2023).

[66] *Verification & validation of computational models associated with the mechanics of materials* (TMS, Pittsburgh, 2019).

[67] A. Stukowski, "Structure identification methods for atomistic simulations of crystalline materials," Modelling and Simulation in Materials Science and Engineering **20,** 045021 (2012).

[68] C. L. Kelchner, S. Plimpton, and J. Hamilton, "Dislocation nucleation and defect structure during surface indentation," Physical review B **58,** 11085 (1998).

[69] A. Stukowski and K. Albe, "Extracting dislocations and non-dislocation crystal defects from atomistic simulation data," Modelling and Simulation in Materials Science and Engineering **18,** 085001 (2010).

[70] A. Stukowski, V. V. Bulatov, and A. Arsenlis, "Automated identification and indexing of dislocations in crystal interfaces," Modelling and Simulation in Materials Science and Engineering **20,** 085007 (2012).

[71] K. Hirokawa, S. Suzuki, K. Abiko, H. Kimura, and M. Oku, "Estimation of the thickness or composition of a covering layer on a solid by XPS or AES," Journal of Electron Spectroscopy and Related Phenomena **24,** 243–253 (1981).

[72] M. Guttmann, P. Dumoulin, and M. Wayman, "The thermodynamics of interactive cosegregation of phosphorus and alloying elements in iron and temper-brittle steels," Metallurgical Transactions A **13,** 1693–1711 (1982).

[73] A. Stukowski, "Visualization and analysis of atomistic simulation data with OVITO–the Open Visualization Tool," Modelling and simulation in materials science and engineering **18,** 015012 (2009).

[74] D. Scheiber and L. Romaner, "Impact of the segregation energy spectrum on the enthalpy and entropy of segregation," Acta materialia **221,** 117393 (2021).

[75] C. Dösinger, M. Hodapp, O. Peil, A. Reichmann, V. Razumovskiy, D. Scheiber, and L. Romaner, "Efficient descriptors and active learning for grain boundary segregation," Physical Review Materials **7,** 113606 (2023).

[76] J. K. Mackenzie and M. J. Thomson, "Some Statistics Associated with the Random Disorientation of Cubes," Biometrika **44,** 205 (1957).

[77] J. K. Mackenzie, "Second Paper on Statistics Associated with the Random Disorientation of Cubes," Biometrika **45,** 229 (1958).

[78] A. Hussein, A. H. Krom, P. Dey, G. K. Sunnardianto, O. A. Moultos, and C. L. Walters, "The effect of hydrogen content and yield strength on the distribution of hydrogen in steel: a diffusion coupled micromechanical FEM study," Acta Materialia **209,** 116799 (2021).

[79] W. Wang, C. Cai, G. S. Rohrer, X. Gu, Y. Lin, S. Chen, and P. Dai, "Grain boundary interconnections in polycrystalline aluminum with random orientation," Materials Characterization **144,** 411–423 (2018).

[80] W. T. Read and W. Shockley, "Dislocation Models of Crystal Grain Boundaries," Physical Review **78,** 275–289 (1950).

[81] D. Wolf, "A Read-Shockley model for high-angle grain boundaries," Scripta Metallurgica Et Materialia **23,** 1713–1718 (1989).

[82] R. Palmer, "Optimization on rugged landscapes," in *Molecular Evolution on Rugged Landscapes*, A. S. Perelson, ed., (CRC Press, Boca Raton, 2018), Chap. 1, pp. 3–25.

[83] J. K. Mason and S. Patala, "Basis functions on the grain boundary space: Theory,", 2019.

[84] S. G. Baird, E. R. Homer, D. T. Fullwood, and O. K. Johnson, "Computationally Efficient Barycentric Interpolation of Large Grain Boundary Octonion Point Sets," MethodsX **9,** 101731 (2022).

[85] D. Raabe, M. Herbig, S. Sandlöbes, Y. Li, D. Tytko, M. Kuzmina, D. Ponge, and P.-P. Choi, "Grain boundary segregation engineering in metallic alloys: A pathway to the design of interfaces," Current Opinion in Solid State and Materials Science **18,** 253–261 (2014).

[86] M. Gong, F. Liu, and Y. Chen, "Modeling solute segregation in grain boundaries of binary substitutional alloys: Effect of excess volume," Journal of Alloys and Compounds **682,** 89–97 (2016).

[87] S. Pal, K. V. Reddy, T. Yu, J. Xiao, and C. Deng, "The spectrum of atomic excess free volume in grain boundaries," Journal of Materials Science **56,** 11511–11528 (2021).

[88] H. J. Frost, F. Spaepen, and M. F. Ashby, "A second report on tilt boundaries in hard sphere F.C.C. crystals," Scripta Metallurgica Et Materialia **16,** 1165–1170 (1982).

[89] A. Sutton and V. Vitek, "On the structure of tilt grain-boundaries in cubic metals II. asymmetrical tilt boundaries," Philosophical Transactions Of The Royal Society Of London Series A-Mathematical Physical And Engineering Sciences **309,** 37–54 (1983).

[90] R. W. Balluffi and P. D. Bristowe, "On the structural unit/grain boundary dislocation model for grain boundary structure," Surface Science **144,** 28–43 (1984).

[91] J. D. Rittner and D. N. Seidman, "$\langle 110 \rangle$ symmetric tilt grain-boundary structures in fcc metals with low stacking-fault energies," Physical Review B **54,** 6999–7015 (1996).

[92] M. A. Tschopp and D. L. McDowell, "Structural unit and faceting description of Sigma 3 asymmetric tilt grain boundaries," Journal Of Materials Science **42,** 7806–7811 (2007).

[93] D. E. Spearot, "Evolution of the E structural unit during uniaxial and constrained tensile deformation," Acta Materialia **35,** 81–88 (2008).

[94] J. Han, V. Vitek, and D. J. Srolovitz, "The grain-boundary structural unit model redux," Acta Materialia **133,** 186–199 (2017).

[95] L. H. Serafin, E. R. Cluff, G. L. W. Hart, and E. R. Homer, "Segregation Energy Spectra of Co in Aluminum Grain Boundaries that span the 5D space of Crystallographic Character,", Mendeley Data, 2024, v1.